③ In the groundwater flow simulation using the hydrogeological model, the horizontal distribution of the drawdown shows a concentric pattern with the shaft as its center. It does not indicate that the Tsukiyoshi Fault forms an impervious zone.

④ The simulation results shows the size of the study area and setting of the boundary conditions used for this simulation could be used for 2nd analysis loop.

4.2.2.6 Future tasks

While the steady-state and transient flow simulations allow understanding the overall groundwater hydrogeology in the study area, none of the investigation results obtained in the area were used for these simulations. The following are extracted as tasks to be dealt with in the future.

① Examine the method of establishing the geological units for the geological model; especially taking the heterogeneity of granite into consideration

② Consider the variety, quantity and quality of information (the data requirements) needed for modeling and groundwater flow simulation

③ Understanding the hydrogeological properties of individual geological units and predict the 3-D distribution of hydraulic conductivity

④ Methodology for construction of the hydrogeological model
Consider the method for estimating 3-D distribution of hydraulic conductivity

⑤ Methodology of groundwater flow simulation
Consider the methods for saturated/unsaturated simulations and the applicability of finite element and finite difference methods.

⑥ Method of setting hydraulic boundary conditions
Consider the method and basis for the top and side boundary conditions, considering the available data

⑦ Assessment of the uncertainty inherent in data obtained, in models and in the groundwater flow simulation
Consider which factors could contribute to reduction of the uncertainty, and, if possible, the prioritization of data acquisition.

4.2.3 Hydrogeological model and groundwater flow simulation (2nd analysis loop)

4.2.3.1 Overview

The groundwater flow simulations carried out for the 2nd analysis loop are based on enhancements to the geological models with data and knowledge from additional hydrological data, borehole investigations in three 1,000 m-deep boreholes (MIU-1, 2 and 3), reflection seismic surveys, and other data to be described below. The borehole investigations consisted of the following:

- Core descriptions and BTV investigations to acquire detailed information on location, orientation and style of fracture zones that are considered to be potential water conducting features (WCF) in the granite

- Hydraulic tests in 100 m-sections (long test intervals) to develop a comprehensive, albeit averaged, database on hydraulic properties from near surface to depth
- Hydraulic tests in sections several metres long (short-test intervals) to establish their hydraulic properties. The specific sections may be potential WCFs, fluid loss zones or major structures.

Based on the results of the above investigations, the geological model for the MIU Project was developed in more detail, with a definition of additional units in the granite (See Section 4.1.4) and their hydrogeological properties were determined for modeling purposes. As a result, the following are made clear.

① The “Upper fracture zone” and “Fracture zone along the fault” have high permeability, whereas the “Moderately fractured zone” has low permeability;

② The piezometric water level in the footwall of the Tsukiyoshi Fault is 20 m higher than that in the hanging wall, suggesting that the fault may be a barrier to flow, which would be a confirmation of earlier work that reached the same conclusion.

Based on the above results, groundwater flow simulations in the 2nd analysis loop for the study area (about 4 km× about 6 km) was carried out with the purpose of understanding changes in hydrogeological properties caused by planned MIU shaft excavation, reassessing the effects of the Tsukiyoshi fault, and examining whether it is necessary to take permeable fractures into consideration.

In the 2nd analysis loop, the following six subjects were to be examined in the development of the hydrogeological model and for the groundwater flow simulation.

① Method of determining the geological units in the geological model

② Data requirements needed for development of the geological and hydrogeological models and the groundwater flow simulation

③ Methodology for construction of the hydrogeological model

④ Groundwater flow simulation methodology

⑤ Method of determining hydraulic boundary conditions

⑥ Assessment of the uncertainty in data, models and the results of groundwater flow simulation

4.2.3.2 Hydrogeological investigations

Hydrogeological investigations are divided into surface hydrological investigations and groundwater hydrogeological survey. The former studies the water budget and infiltration mechanism of the surface water, whereas the latter studies the distribution of hydraulic conductivities and pore pressures in the deep rock mass, flow paths of groundwater and their continuity.

4.2.3.2.1 Surface hydrological investigations

Water balance observations have been carried out in the Shobasama Site to establish the top boundary conditions required for groundwater flow simulation. To evaluate the water balance around the Shobasama Site, results of the meteorological and groundwater observations carried out in the RHS Project can be used.

Results of the subsurface hydrological investigations carried out in both the RHS Project and this project are as follows.

(1) Water budget

The map of the drainage basins identified for water budget determination carried out in the MIU Project and the RHS Project are shown in Figure 4.37. Table 4.14 provides details on watershed characteristics. The drainage basins were established taking their topography, geology, relative location and scale into consideration [57]. Observation devices installed for the RHS Project in the drainage basin of the Shoba River can be used for the water balance calculations for the MIU Project.

Table 4.14 Details of hydrological monitoring network used for the MIU Project

River			Drainage basin		Fluvio Meter	Lithology	Catchment area (ha)	Elevation (m)	Observation period
Toki River	Hiyoshi River	Shoba River	Shoba River	Shoba River	SPD	Toki Gravel, Sedimentary rocks	53.5	(224)	1989.4.21-
				Upper stream	SPU		15.5	(253)	1989.4.21-
				Itadoribora River	IPU		1.2	(267)	1993.3.6-
			Shoba River model*		SPM		1.5	262	1998.12.24-
		Garaishi River	Garaishi River	Garaishi River	GPD	Toki Gravel	23.3	(296)	1999.3.20-
				Minor	GPU	Granite	1.0	(342)	1999.5.26-
	Shizuhora River		Tono Mine		TPU	Toki Gravel, Sedimentary rocks	6.2	(257)	1990.9.18-2000.2.17

* carried out in the MIU Project (all others were carried out in the RHS Project)

Infiltration rates of the rock mass are converted to estimated yearly ranges based on the observation results in the individual drainage basins obtained for the past ten years. These are 0.3 to 1.0 mm/day (0.6 mm/day on average) in the Shoba River drainage basin and 0.1 to 1.8 mm/day (1.0 mm/day on average), in the upper streams of the Shoba River drainage basin. It indicates that there are spatial and temporal variations within individual basins. The infiltration rate in the Garaishi River basin, which is underlain by granite and located to the north of the Shobasama Site, was determined to be 0.2 mm/day according to observations in 1999 FY. It is necessary to establish a methodology for determining the infiltration rates of each basin by examining the correlation of infiltration rates into the rock mass with topography, geology and land utilization.

(2) Groundwater monitoring

Groundwater monitoring is intended to provide data on the fluctuations of water level in unconsolidated layers (Seto Group) and sedimentary rocks (Mizunami Group) with which to directly estimate recharge rates. Locations of groundwater observatories for the MIU Project and the RHS Project are shown in Figure 4.38. Open-air-type water level gauges are used for measuring water level in open boreholes, while soil moisture meters are used in soil and the upper part of the Seto Group.

Groundwater observations of the MIU Project were carried out in the six boreholes shown in Table 4.15 [58, 59]. In this study area, there are also the TH-series-boreholes, the SN-series-boreholes and the AN-6 borehole around Tono Mine, in which continuous observations on water level and water pressure are under way with either open-air-type water gauges or multiple piezometer systems (MP system) [60].

Table 4.15 Details of water level monitoring for the MIU Project

Borehole	Target geology	Location and sensitivity to rainfall
AI-4	Weathered part of granite ～ Lowest part of Toki Lignite-bearing Fm.	・The vicinity of planned shaft in the Shobasama Site ・Hardly sensitive to rainfall
97MS-01	Upper part of Akeyo Fm.	・Ridge on the Shoba River drainage basin ・Sensitive only to heavy rain
97MS-02	Lower part of Seto Group	・Ridge on the Shoba River drainage basin ・Sensitive to rainfall
98MS-03	Middle part of Akeyo Fm.	・Ridge on the Shoba River drainage basin ・Not sensitive to rainfall
98MS-04	Lower part of Seto Group	・Slope in the Shoba River drainage basin ・Sensitive to rainfall
99MS-05	Lower part of Akeyo Fm.	・Slope in the Shobasama Site, southward from planned shaft ・Sensitive to rainfall, if not less sensitive than Seto Group

Soil moisture observations are carried out at two locations [59] in the Shoba River basin (Table 4.16) with the purpose of estimating the water movement through the unsaturated zone layers into the saturated zone. From these observations, local recharge rates can be estimated. Outside the study area, groundwater observations are under way at 12 stations in the Itadori-bora and Tono Mine drainage basins.

Table 4.16 Details of soil moisture monitoring in the MIU Project

Tensiometer	Target geology	Location and sensitivity to rainfall
SmTP	Soil～ Upper part of Seto Group	・Located on ridge ・Became saturated 7 months after installation, but inconsistent with groundwater level (＞3 m).Since then, become sensitive even to light (4 mm) rainfall (＜2) ・No response except for heavy rain (＞3m)
SmTS	Soil～ Upper part of Seto Group	・Located in slope ・Become saturated 3months after installation (＞5m). ・Sensitive to rainfall (＜1.5 m), whereas no response except for heavy rain (＞2 m)

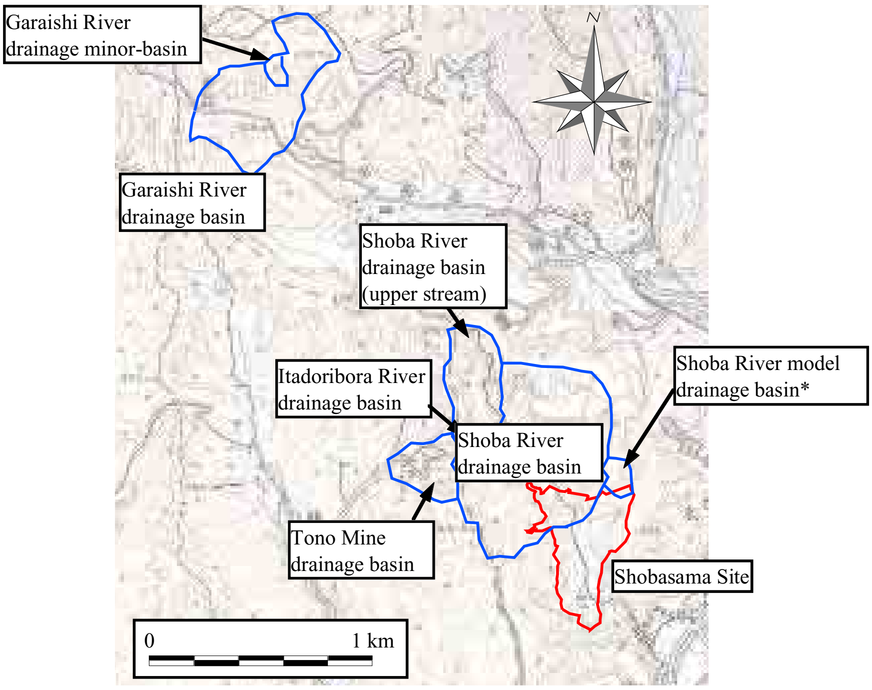

1:50,000 "Minokamo" published by Geographical Survey Institute

Figure 4.37 Drainage basins for the water budget determination in the MIU Project* and the RHS Project

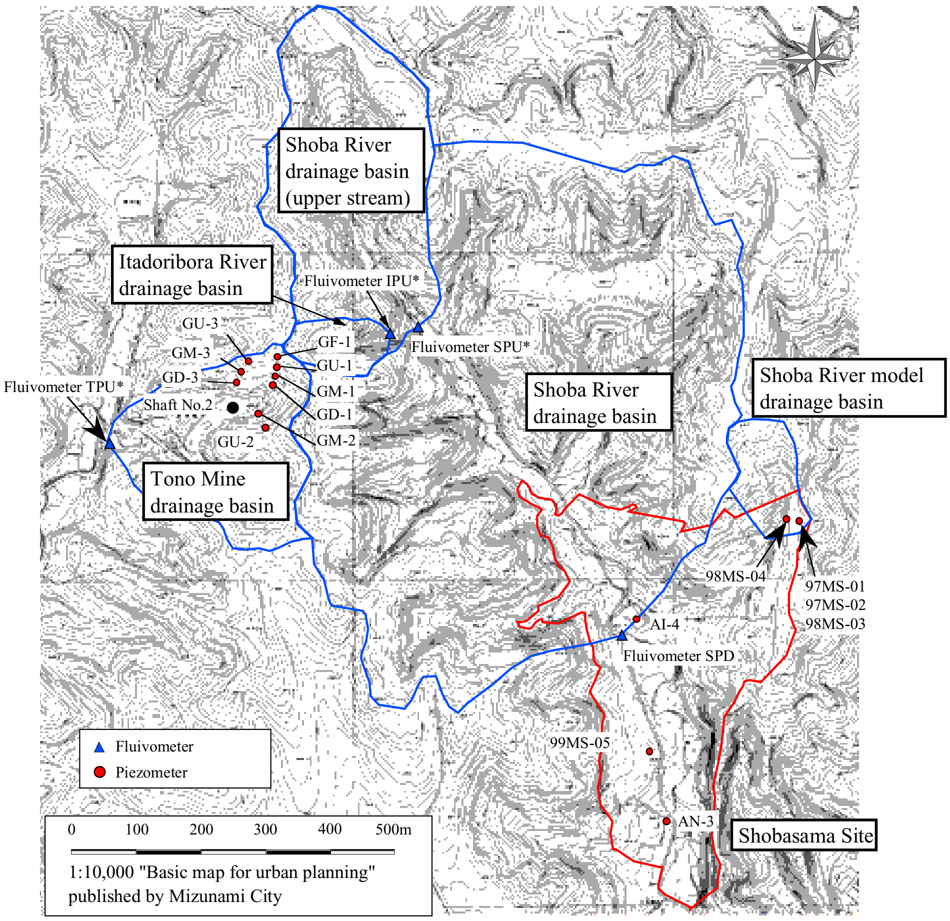

Figure 4.38 Location map of groundwater observatories and the water level monitoring on the MIU Project* and the RHS Project

Infiltration rates of rainfall into the soil and the underlying weathered part of the Seto Group, which cover the surface of hills, have yet to be understood quantitatively due to developmental status of the measuring technique to determine soil moisture. On the other hand, groundwater stored in the Seto Group, which occupies the upper half of hills surrounding the Shobasama Site, is thought to form the base flow of the Shoba River and others [58, 61].

In the Mizunami Group, an unsaturated zone develops, which produces confined groundwater separated from the groundwater in the overlying Seto Group. Furthermore, the heterogeneous distribution of geological formations in the Mizunami Group generates a heterogeneous distribution of water pressures within it [58, 62, 63].

4.2.3.2.2 Groundwater hydrogeological survey

The "Groundwater hydrogeological survey" refers to investigations to understand hydrogeological properties of the rock mass using boreholes exceeding several hundred meters in depth. While the drilling of the MIU-1, 2 and 3 were in progress in the Shobasama Site, hydraulic tests were carried out to determine flow system characteristics such as hydraulic conductivity [39, 40, 41]. The methods used and number of hydraulic tests performed are shown in Table 4.17. Crosshole hydraulic testing between MIU-2 and 3 were carried out to confirm whether the Tsukiyoshi Fault acts as a hydraulic barrier to flow and to obtain data on the continuity and physical properties of the "Fracture zone along the fault" [64].

Table 4.17 Details of hydraulic tests

Borehole		Depth (m)	Details	Tests
MIU Project	MIU-1 (39)	1,011.8	Pulse/slug tests were carried out for both fracture zones and intact rock, with 6.5 m test intervals. Also, pumping tests were carried out continuously in 100 m long test intervals.	Pulse/slug:28 Pumping:9
	MIU-2 (40)	1,012.0	Same as MIU-1. In addition, flow rates in pumping test were carefully controlled. Also, timing for pumping test completion was being improved.	Pulse/slug:30 Pumping:8
	MIU-3 (41)	1,014.0	Pulse/slug tests with several to several tens of meters intervals were carried out to study fractures (zones). Pumping tests with intervals up to 100 m were carried out. The test intervals were set according to fracture distributions. Also, flow rates in pumping test were carefully controlled. Adopting derivative plots of change in water pressure enhanced reliability of analysis data.	Pulse/slug:23 Pumping:11
Other geoscientific research	AN-1	1,010.2	Drilling of these AN-series boreholes was carried out from 1986 to 1988. Test intervals of 2 to 3 m were used to target mainly the fractures (zones).	Pulse/slug:34
	AN-3	408		Pulse/slug:24
	DH-2 (55)	501	Pulse/slug tests were carried out for both fracture zones and intact rock, with 2 to 8 m long test intervals.	Pulse/slug:10
	DH-4	505		Pulse/slug:9
	DH-9 (65)	1,030.0	Pulse/slug tests were carried out in 6.5m test intervals. Pumping test was in an 80 m test interval. Test intervals include fracture (zone), intact granite and anomalies detected by physical logging.	Pulse/slug:5 Pumping:1
	DH-11 (66)	1,012.0	Pulse/slug tests were in 10 m test intervals to target groundwater flowpaths. Pumping tests were carried out in 40 to 116 m long test intervals to cover the entire hole.	Pulse/slug:3 Pumping:8

MP borehole completion systems were installed in boreholes for continuous observation of water pressure and water chemistry after the MIU excavations. In the Shobasama Site, drilling and investigations in the AN-series of boreholes were carried out prior to investigations in the MIU-series boreholes. In addition to using the information obtained by these investigations, the MP systems were installed in the AN-series of boreholes to obtain new data on the pressure and water chemistry. Table 4.18 shows timetable of actual drilling and investigations in the boreholes in the Shobasama Site (MIU-1, 2 and 3, AN-1 and 3) and the DH-series of boreholes drilled for the RHS Project.

Table 4.18 Timetable of drilling and investigations

Borehole		～1997	1998	1999	2000
MIU Project	MIU-1				MP*
	MIU-2				MP* Crosshole Hydraulic test
	MIU-3				
Other Geoscientific research	AN-1	1986. 7～1988. 4			MP*,**
	AN-3	1987. 7～1987. 9			MP*,**
	DH-2	1994.12～1994. 3			
	DH-4	1994.11～1995. 3			
	DH-9				
	DH-11				

* Hydraulic observation using MP system, ** carried out in the MIU Projects

Results of the long-interval pumping tests carried out in the MIU-1, 2 and 3 shown in Figure 4.39 are expressed as vertical distribution of hydraulic conductivity with depth. The basal conglomerate of the Toki Lignite-bearing Formation, the weathered part of the granite, “Upper fracture zone”, “Moderately fractured zone”, “Fracture zone along the fault” and the Tsukiyoshi Fault are considered the geological features controlling the groundwater hydrogeology. Results of hydraulic tests (pulse/slug tests) and pumping tests indicate that the hydraulic conductivity of the “Moderately fractured zone” is about an order of magnitude lower than the “Upper fracture zone” and “Fracture zone along the fault” (Figure 4.40).

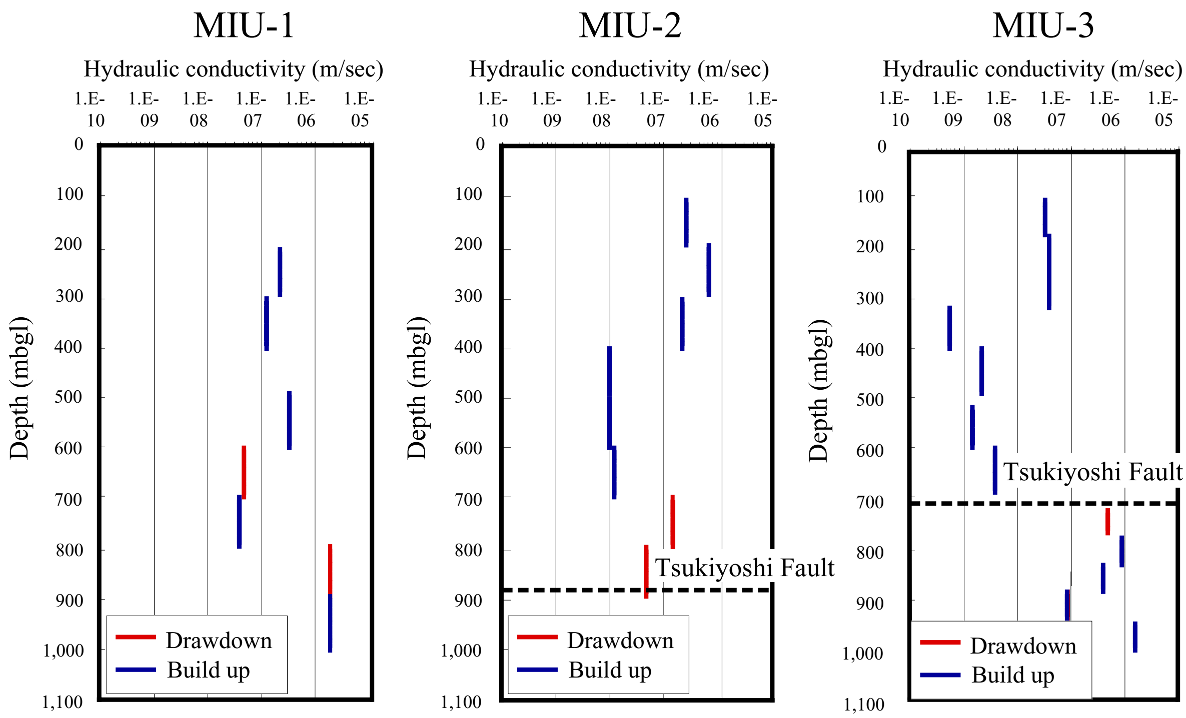

Figure 4.39 Hydraulic conductivity based on the pumping test

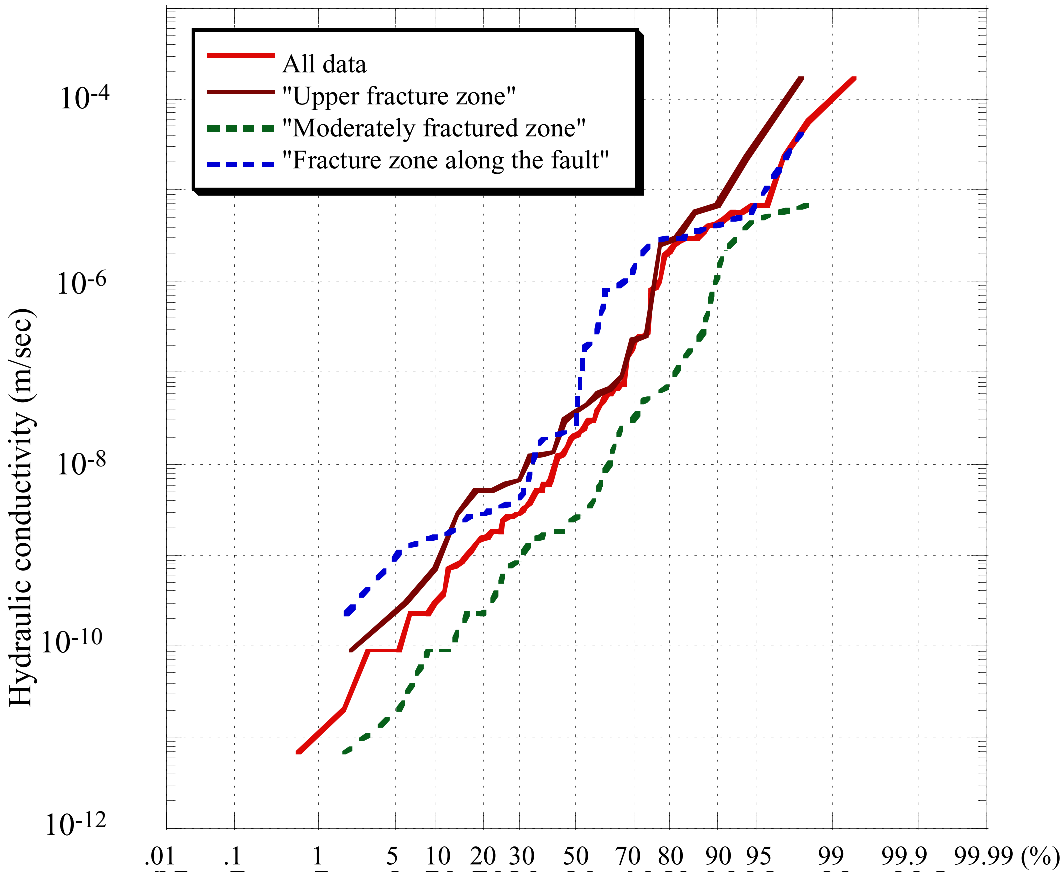

Figure 4.40 Hydraulic conductivity of MIU-1~3

An example of the pore water pressure distribution in the Shobasama Site is shown in Figure 4.41. The pore water pressures are measured in isolated sections in MIU-1, 2 and 3. The largest pressure difference is recognized between the measuring sections on opposite sides of the Tsukiyoshi Fault. The fault is intersected by MIU-2 at an elevation of -650 masl as shown in the correlation graph between elevation and pore pressure and at the No.26 measuring section shown in the water level histogram, respectively. The nos.1 to 3 measuring sections, which are characterized by a high pore pressure decreasing with depth, correspond with the distribution of the Akeyo Formation (consisting of mudstone, sandstone and conglomerate). This suggests that the mudstone and sandstone in the formation are low in permeability and form a hydraulic barrier to flow. The fact that the Akeyo Formation in the Shobasama Site has a higher pore pressure is ascertained in the 99MS-05 borehole drilled for the surface hydrological survey.

In general, the pore pressure in the MIU-2 is higher and more variable with depth than in the MIU-1. As for the pore pressure in the MIU-3, it has a tendency similar to that in the MIU-2 though it is affected by the pressure release of the MIU-2. The clarification of temporal change in pore pressure and the observation on annual/seasonal variations in pore pressure behavior as well as hydrogeological effects of borehole excavations are in progress.

4.2.3.3 Hydrogeological model and groundwater flow simulation (study area)

4.2.3.3.1 Overview

Based on the results of the hydrogeological investigations and the problems to be solved in the 2nd analysis loop, a groundwater flow simulation was carried out [67] using the model described below. The aim was to test the hydrogeological model and methodology for the groundwater flow simulations. This model expresses the heterogeneous distribution of physical properties (due to structural discontinuities) of the rock mass, by an equivalent continuum. This model is called the equivalent continuum model.

4.2.3.3.2 Setting of the study area

The study area is identical with that modeled in the 1st analysis loop (about 4 km× about 6 km encompassing the Shobasama Site at its center).

4.2.3.3.3 "Equivalent Continuum Model"

This model allows expressing discontinuous and heterogeneous hydrogeological properties in the rock mass by dividing the study area into finite elements and by computing permeability tensors of the individual finite elements from the information on fracture distribution. Unlike the fracture network model dealing with each fracture, this model sets an equivalent physical value (permeability, etc.) in response to fracture density in each mesh. Therefore, this model is suitable for groundwater flow simulation of several km square fractured rock masses.

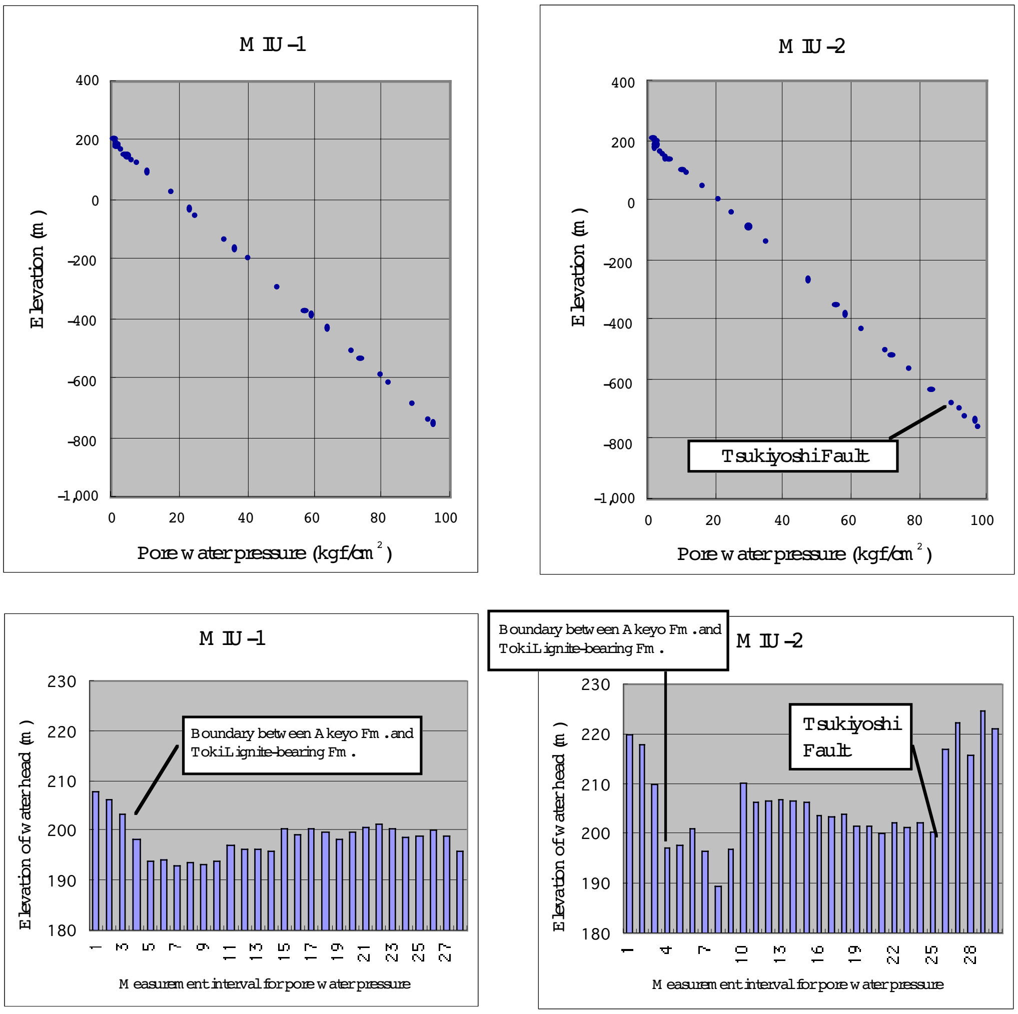

Figure 4.41 Pore water pressure distribution at the MIU-1, MIU-2

4.2.3.3.4 Hydrogeological model

(1) Procedure for model construction

The model development procedure for groundwater flow simulations is shown in Figure 4.42. Based of geological units and the results of hydrogeological investigations (See Section 4.2.3.2), "equivalent continuum model" is constructed for the study area (about 4 km × about 6 km).

A statistical processing of fractures is applied to three units, the "Upper fracture zone", the "Moderately fractured zone" and the "Fracture zone along the fault". As in the 1st analysis loop, a unique physical value is assigned to each of the sedimentary rock formations, the weathered granite and the Tsukiyoshi Fault, thus they are treated as a homogeneous continuum. For the sedimentary rocks and the Tsukiyoshi Fault, statistical treatment is not applied because sufficient detail on the fracture network systems did not exist for them. The deeply weathered part of the granite is not only lacking details on fracturing and hydraulic character but also is so porous due to weathering and alteration that it is treated as a uniform zone with unique physical properties. As a result, it is not included in the statistical processing of fractures.

(2) Generation of fracture network model

The construction of "equivalent continuum model" requires determining the statistical distribution of geometrical azimuth, aperture and radii of fractures. The 3-D fracture density is also required. Particularly, hydraulic apertures must be used instead of geometrical ones observed on the walls of the rock mass or boreholes.

Figure 4.43 shows the process of generation of a fracture network model. The main process is as follows.

- Identify open fractures which are generally presumed highly permeable, based on results of BTV investigations
- Determine their orientations (n), intensities (1-D fracture density) in boreholes (ρ_1) and geometrical apertures (t_g)
- Carry out virtual permeability tests simulating hydraulic tests in boreholes.
- Estimate the averages of radii (r) and hydraulic apertures (t_h) of fractures by comparing simulated and measured values of hydraulic conductivities
- Calculate 3-D densities (ρ_3) by inputting a mean square value of fracture diameter and ρ_1 into a geometrical relational expression of fracture.

Derivation of statistical values of fractures

Orientation (n)

Using a cluster analysis of the orientations of all fractures intersected by the BTV survey, fractures in the "Upper fracture zone" are divided into four sets with the following major attitudes: (1) low angle fractures; (2) N50-70E, dip 70-80SE; (3) N80-90W, dip 60-70N; and (4) N20-50E, dip 70-80SW. Based on the cluster analysis, fractures are divided into groups on a Schmidt diagram and fracture orientations within the groups are defined by using a Bingham distribution. Parameters of fractures (Figure 4.44) are shown in Table 4.19.

The Fisher distribution (hemispheric normal distribution) has been most popular as a statistical model to express orientations of fractures in the rock mass. The Fisher distribution is characterized by an isotropic distribution around the center of dominant orientation. On the other hand, the Bingham distribution is characterized by an anisotropic distribution and allows modeling an elliptic or belt-shaped distribution. Orientations of fractures intersected by MIU-1, 2 and 3 are not always isotropic, suggesting constraints on the reproduction of data by the Fisher distribution. Thus, the Bingham distribution was employed for modeling orientations of fractures.

Intensities (1-D fracture density) (ρ_1)

The total fracture population detected by BTV surveys in all MIU boreholes is 10,369. However, of the total fracture population, only 188 are clearly open fractures, representing 1.8% of the total. The 1-D densities of total fracture population and the open fractures are shown for the four major orientation sets in the individual zones in Table 4.19.

Table 4.19 Fracture density according to the results of the BTV investigations

	Interval	Frequency	Total Fracture density (n/m)	Open fracture density (n/m)
"Upper fracture zone"	Set-1	1,911	2.479	0.045
	Set-2	341	0.442	0.008
	Set-3	484	0.628	0.011
	Set-4	732	0.949	0.017
	Total	3,468	4.498	0.082
"Moderately fractured zone"	Set-1	839	0.755	0.014
	Set-2	461	0.451	0.008
	Set-3	538	0.484	0.009
	Set-4	583	0.524	0.010
	Total	2,421	2.177	0.039
"Fracture zone along the fault"	Set-1	1,670	1.888	0.034
	Set-2	809	0.915	0.017
	Set-3	1,128	1.275	0.023
	Set-4	873	0.987	0.018
	Total	4,480	5.066	0.092

Geometrical aperture (t_g)

Using the data on aperture of open fractures determined from the BTV investigations, the relationships between apertures and 1-D fracture densities (the total number of open fractures with openings less than a given value) are examined. The results are shown in Table 4.20.

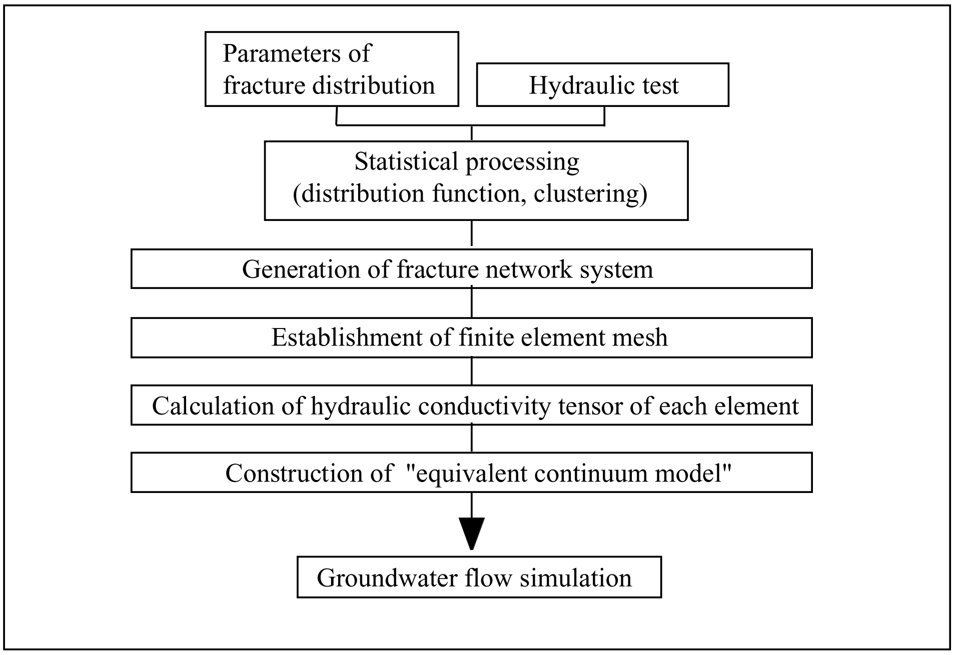

Figure 4.42 Procedure for construction of the "equivalent continuum model"

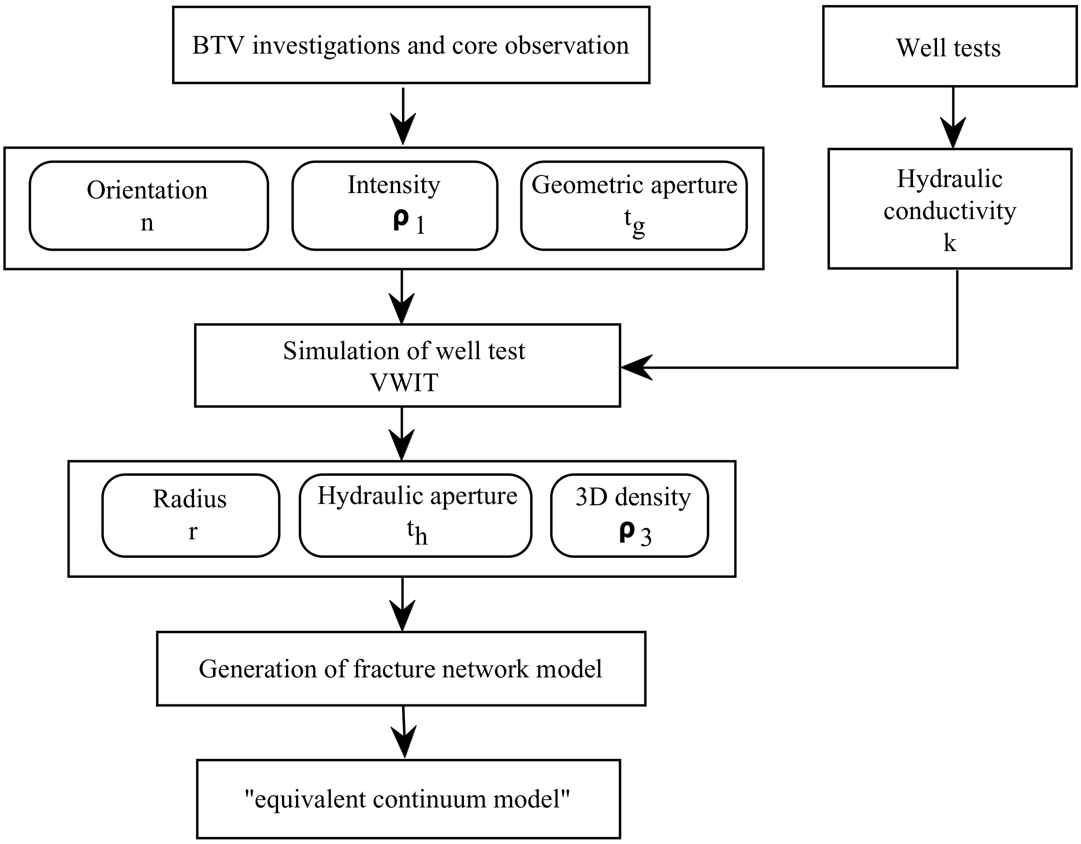

Figure 4.43 Flow diagram for determination of fracture statistics for equivalent heterogeneous continuum modeling

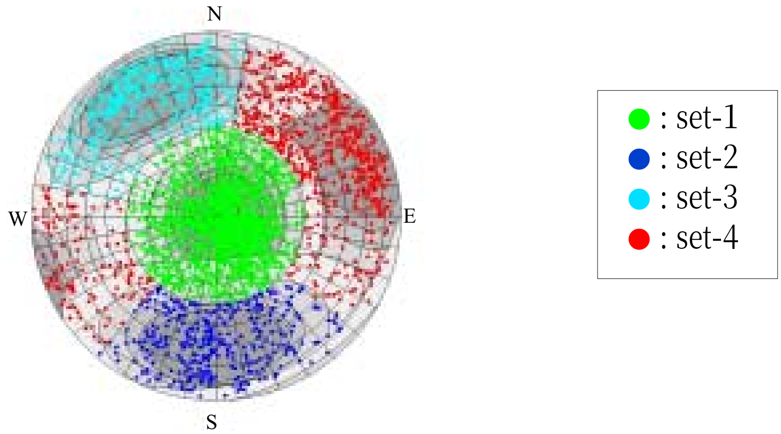

(a) "Upper fracture zone"

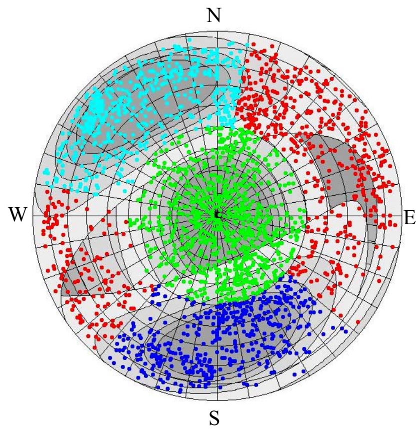

(b) "Moderately fractured zone"

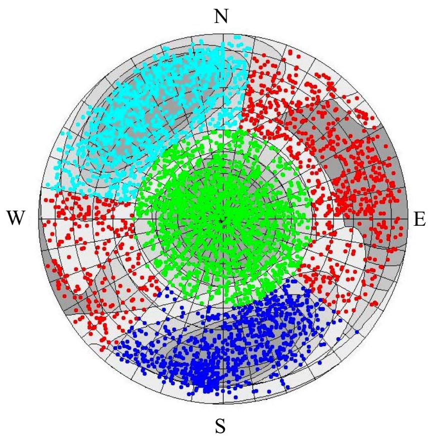

(c) "Fracture zone along the fault"

Figure 4.44 Lower hemisphere stereonet projection for three zones

Table 4.20 Relationship between aperture and fracture density of the MIU-1, 2 and 3

Aperture(mm)	Frequency	Cumulative percentage (%)	Cumulative frequency	Fracture density (n/m)
0.0	60	100.00	188	0.0688
0.5	15	68.09	128	0.0468
1.0	42	60.11	113	0.0413
1.5	21	37.77	71	0.0260
2.0	10	26.60	50	0.0183
2.5	15	21.28	40	0.0146
3.0	4	13.30	25	0.0091
3.5	4	11.17	21	0.0077
4.0	4	9.04	17	0.0062
4.5	4	6.91	13	0.0048
5.0	2	4.79	9	0.0033
5.5	1	3.72	7	0.0026
6.0	2	3.19	6	0.0022
6.5	1	2.13	4	0.0015
7.0	1	1.60	3	0.0011
7.5	0	1.06	2	0.0007
8.0	0	1.06	2	0.0007
8.5	0	1.06	2	0.0007
9.0	0	1.06	2	0.0007
9.5	0	1.06	2	0.0007
10.0	0	1.06	2	0.0007
>10.0	2	1.06	2	0.0007

Generation of fracture network model by virtual permeability tests

Virtual permeability tests

Virtual permeability testing is a trial-and-error method to determine fracture statistics (fracture radius, hydraulic aperture and 3-D fracture densities) through numerical simulations of hydraulic tests. From the fracture statistics, distribution of hydraulic conductivity was calculated as if actual permeability tests were carried out. The method for derivation of fracture radii, hydraulic apertures and 3-D densities used in the computing process is shown in Figure 4.45.

Distribution of hydraulic conductivity

Results from single-borehole permeability tests carried out in MIU-1, 2 and 3 were used for comparison with results of the virtual permeability tests. Figure 4.40 shows distributions of hydraulic conductivities obtained by permeability tests carried out in the granite. The results indicate that measured hydraulic conductivities roughly have a log-normal distribution. These hydraulic conductivities extend over a numerical range exceeding 8 orders of magnitude, indicating an extremely high heterogeneity. Also, the results indicated that the hydraulic conductivity of the “Moderately fractured zone” is nearly an order of magnitude lower than those of the “Upper fracture zone” and “Fracture zone along the fault”. The virtual permeability tests (described below) compute the fracture distribution parameters that allow reproducing these tendencies.

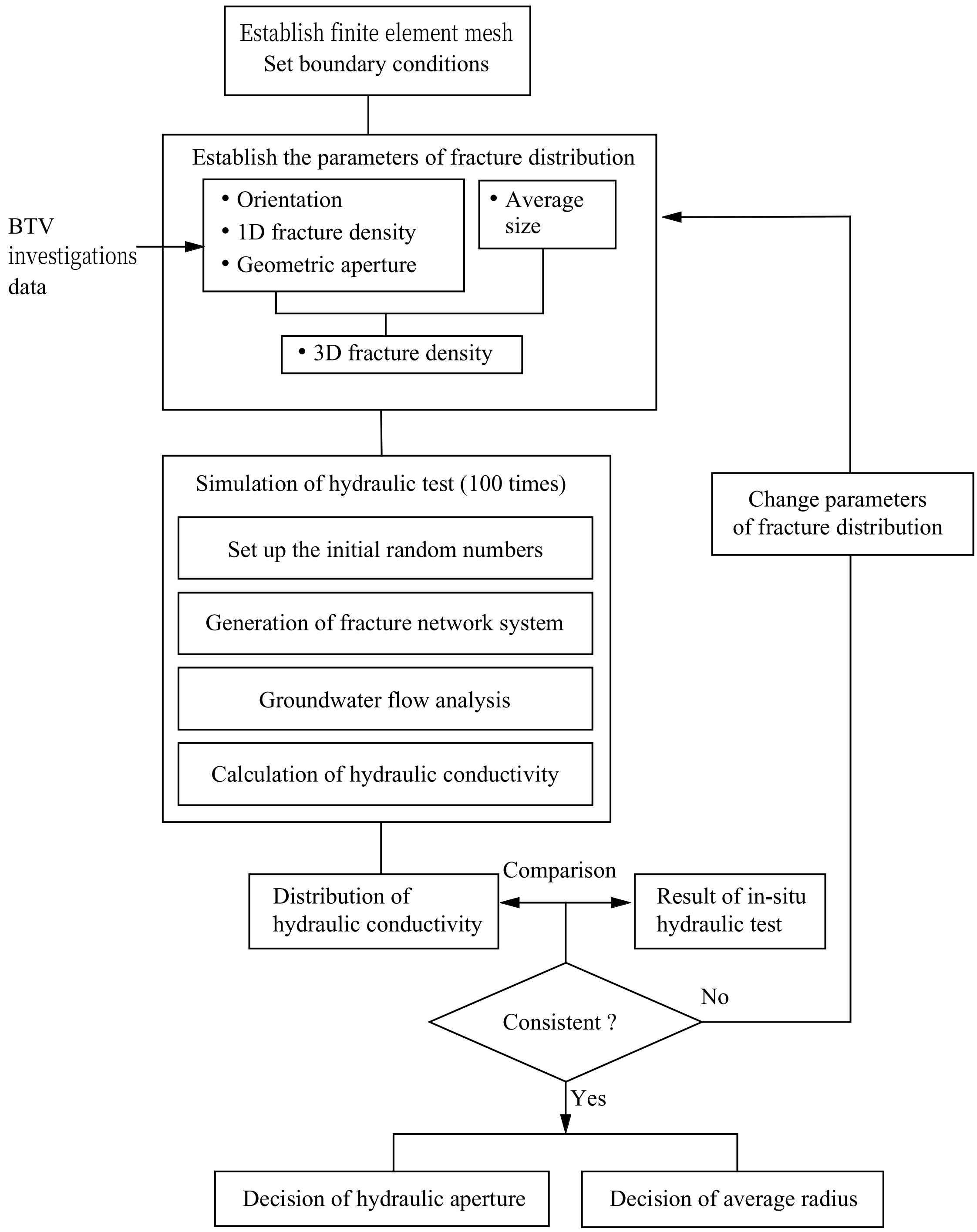

Figure 4.45 Procedure of virtual water injection test (VWIT)

Virtual permeability tests

Given 1-D fracture densities and fracture radii distribution (or diameter distribution), 3-D fracture densities are obtained by the following equation:

$$\rho_3 = \frac{4}{\pi} \cdot \frac{\rho_1}{\left\langle d^2 \right\rangle}, \qquad (4.2.1)$$

ρ_1: 1-D fracture density, ρ_3 : 3-D fracture density, $\left\langle d^2 \right\rangle$: a mean square of fracture diameter

In the identification of parameters by virtual permeability tests, it is confirmed whether or not the tests can express the groundwater hydrogeology, on the following assumptions.

① Only open fractures are employed to determine the 1-D fracture distribution.
Open fractures are generally thought to control groundwater hydrology.

② Aperture of fractures shows a negative exponential distribution. One distribution parameter is applied to all of the fracture sets.
Open fractures in the individual fracture groups are too few to provide meaningful statistical information. Therefore, not only to all open fractures but also to the individual groups of fractures, is a negative exponential distribution of aperture applied.

③ The Bingham distribution is applied to the orientation distribution of the individual fracture groups.
The Bingham distribution is employed to express an anisotropic tendency of the fracture distributions.

④ The following truncated power law distribution and negative exponential distribution are assumed to express the distribution of fracture radii. Irrespective of fracture groups, one distribution parameter is applied to a group.
Power distribution and negative exponential distribution are applied on the basis of the existing studies [68, 69].

$$f(r) = \frac{b-1}{r_{\min}} \cdot \left[\frac{r_{\min}-1}{r}\right]^b, \quad r \geq r_{\min} \quad (b=3)$$

$$f(r) = \lambda \cdot \exp(-\lambda r), \quad \text{but} \quad \lambda = 1 / \langle r \rangle$$

r : fracture radius, $r_{\min}$: minimum fracture radius, b : power number, $\langle r \rangle$: average of fracture radii

In the modeling of fracture radii by a truncated power law distribution and a negative exponential distribution, the mean square of fracture diameters $\left\langle d^2 \right\rangle$ are obtained by the following equations.

・Truncated power law distribution

$$\left\langle d^2 \right\rangle = (b-1)(2r_{\min})^2 \{\ln(2r_{\max}) - \ln(2r_{\min})\},$$

・Negative exponential distribution

$$\langle d^2 \rangle = \frac{1}{\lambda}\left\{\exp(-\lambda d_{\min})\cdot\left(\lambda^2 d_{\min}{}^2 + 2\lambda d_{\min} + 2\right) - \exp(-\lambda d_{\max})\cdot\left(\lambda^2 d_{\max}{}^2 + 2\lambda d_{\max} + 2\right)\right\}$$

r_{max} : maximum fracture radius, d_{min} : minimum fracture diameter, d_{max} : maximum fracture diameter

The $<d^2>$ is very dependent on r_{min} in truncated power law distribution and λ in negative exponential distribution, respectively.

⑤ There is a linear proportional correlation between geometrical and hydraulic apertures.

No tracer test was carried out, therefore, hydraulic aperture could not be verified. At the time it was thought to be the most conservative for analytical purposes to assume that geometrical apertures continue without change by neglecting any possible irregularities of fractures.

・Truncated power law model

The prediction of 3-D open fracture density (ρ_3) based on 1-D open fracture density (ρ_1) from Equation (4.2.1) failed to completely reproduce the measured distributions of hydraulic conductivities which have a range of up to 8 orders of magnitude, as shown in Figure 4.46. It is difficult to have the entire measured dataset, with such a wide distribution range, match with the truncated power law model. Therefore, it will be necessary to devise a method (e.g. fit the measured data for the individual geological units with the model). The present simulation adopts the truncated power law model, employing r_{min} = 70 m and r_{max} = 3,000 m, which shows the best match between measured and computed data. In this case, 1-D density of open fractures is taken into consideration, and the linear (log-normal) distribution of measured data is retained.

・Negative exponential model

The main aim of simulation is to reproduce the heterogeneity of measured hydraulic conductivities. The simulation, following the procedure shown in Figure 4.43, and which used open fractures detected by BTV investigations, failed to achieve a good match between measured and computed values. Accordingly, it was attempted to find fracture distribution parameters that allow computed values to approach the measured values by changing 1-D fracture densities. The simulation indicated that the distribution of hydraulic conductivity is hardly affected by the value of r_{ave} under a constant value of $<d^2>$ in the negative exponential model. Thus, the effect of reducing the 1-D fracture density (ρ_1) was examined with a fixed value of r_{ave}=80 m. As a result, it turned out that the effect of a change in ρ_1 on the heterogeneity of hydraulic conductivity distribution is larger than that of the average fracture radius (r_{ave}) in the truncated power law model. However, too small a value of ρ_1 often results in hydraulic conductivity values ranging from 10^{-11} to 10^{-10} m/s. In this case, the distribution of hydraulic conductivity deviates significantly from a log-normal distribution (Figure 4.47). Thus, the comparison with the distribution of measured hydraulic conductivity justifies adopting r_{ave}=80 m and ρ_1=0.0049 for the negative exponential model.

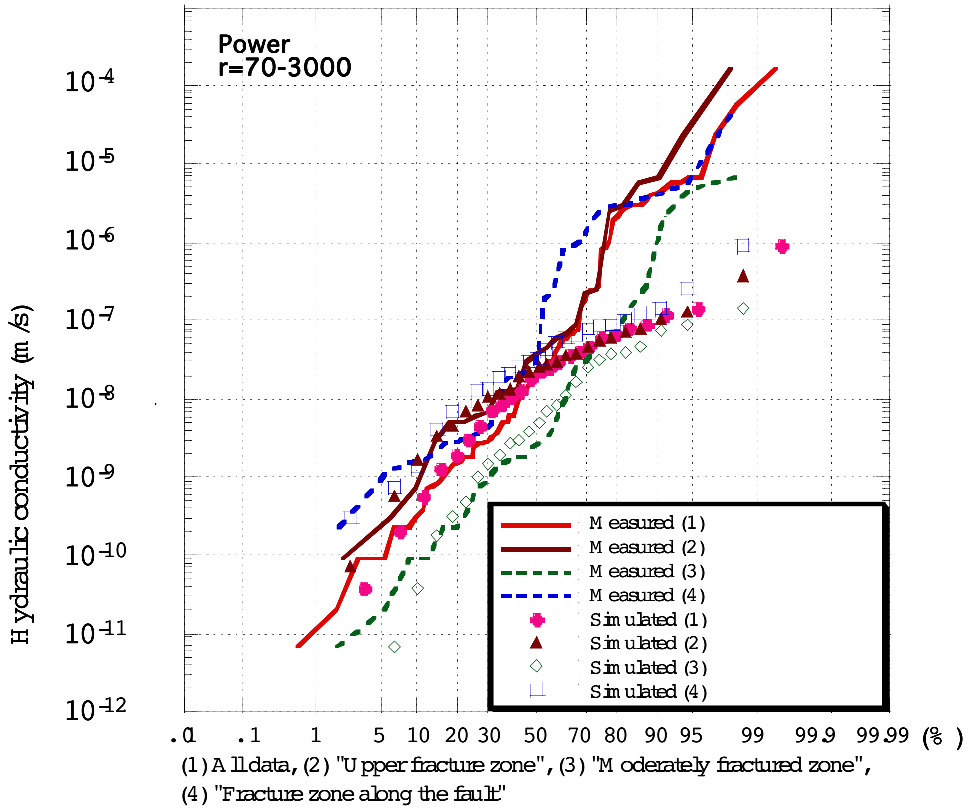

Figure 4.46 Cumulative plot of the hydraulic conductivity (MIU-1~3)
(Truncated power law model)

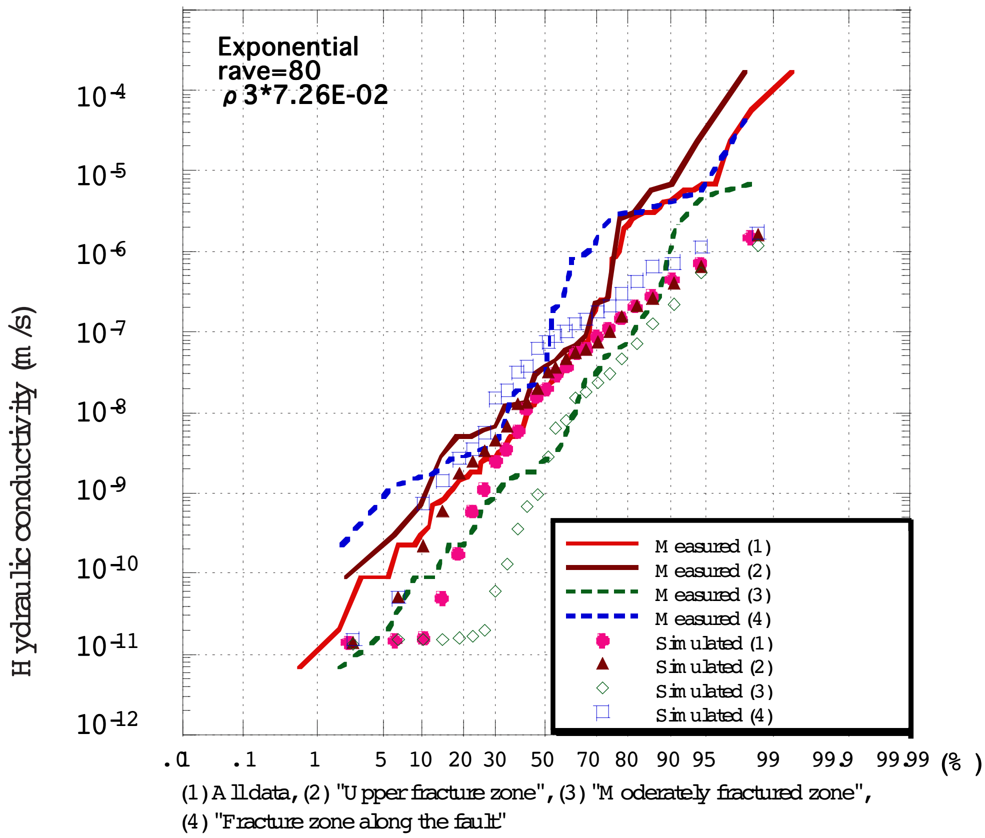

Figure 4.47 Cumulative plot of the hydraulic conductivity (MIU-1~3)
(Negative exponential model)

These two distribution models are summarized in Table 4.21. Comparing the two models, average fracture diameters and 3-D fracture densities are almost similar. However, Model 1 has a larger distribution range of fracture radii and a higher 1-D fracture density. Thus, the latter is characterized by lower fracture continuity and higher heterogeneity of hydraulic conductivity.

Table 4.21 Details of fracture models

		r_{min}	r_{max}	r_{ave}	$\langle d \rangle$	$\langle d^2 \rangle$	ρ_1	ρ_2
Model 1	Truncated power law	70 m	3,000 m	—	137m	1.47×10^5 m^2	6.79×10^{-2}	5.87×10^{-7}
Model 2	Negative exponential	—	—	80 m	160 m	1.28×10^4 m^2	4.9×10^{-3}	4.91×10^{-7}

Summary

Fracture distribution parameters determined by the above statistical derivations are listed in Tables 4.22 and 4.23. Fracture densities (ρ_1, ρ_3) in the individual zones are calculated using whole fracture densities simulated for the above models and the fracture ratio in the sets shown in Table 4.19. On the assumption that hydraulic aperture is proportional to geometrical aperture, a proportionality constant is set so that logarithmic means of both in-situ permeability tests and virtual permeability tests become equal.

Figures 4.46, 4.47 show comparison between simulated distributions of hydraulic conductivity and the measured values in the each model.

Table 4.22 Parameter of statistical fracture distribution
(Truncated power law model)

	Set	Fracture density ρ_1 (n/m)	Mean geometrical aperture t_g(m)	Mean hydraulic aperture t_h(m)	Mean fracture radius r_{ave}(m)	Volumetric fracture density ρ_3(1/m^3)
"Upper fracture zone"	1	4.49×10^{-2}	1.70×10^{-3}	7.91×10^{-5}	70	3.88×10^{-7}
	2	8.02×10^{-3}				6.39×10^{-8}
	3	1.14×10^{-2}				9.84×10^{-8}
	4	1.72×10^{-2}				1.49×10^{-7}
"Moderately fractured zone"	1	1.37×10^{-2}	1.70×10^{-3}	7.91×10^{-5}	70	1.18×10^{-7}
	2	7.52×10^{-3}				6.50×10^{-8}
	3	8.77×10^{-3}				7.58×10^{-8}
	4	9.51×10^{-3}				8.22×10^{-8}
"Fracture zone along the fault"	1	3.42×10^{-2}	1.70×10^{-3}	7.91×10^{-5}	70	2.96×10^{-7}
	2	1.66×10^{-2}				1.43×10^{-7}
	3	2.31×10^{-2}				2.00×10^{-7}
	4	1.79×10^{-2}				1.55×10^{-7}
PDFs		Bingham	Negative exponential	Negative exponential	Negative exponential	Truncated power law

Table 4.23 Parameter of statistical fracture distribution (Negative exponential model)

	Set	Fracture density ρ_1 (n/m)	Mean geometrical aperture t_g(m)	Mean hydraulic aperture t_h(m)	Mean fracture radius r_{ave}(m)	Volumetric fracture density ρ_3(1/m^3)
"Upper fracture zone"	1	3.26×10^{-3}	1.70×10^{-3}	1.70×10^{-4}	80	3.25×10^{-7}
	2	5.82×10^{-4}				5.79×10^{-8}
	3	8.26×10^{-4}				8.22×10^{-8}
	4	1.25×10^{-3}				1.24×10^{-7}
"Moderately fractured zone"	1	9.93×10^{-4}	1.70×10^{-3}	1.70×10^{-4}	80	9.88×10^{-8}
	2	5.46×10^{-4}				5.43×10^{-8}
	3	6.37×10^{-4}				6.33×10^{-8}
	4	6.90×10^{-4}				6.86×10^{-8}
"Fracture zone along the fault"	1	2.49×10^{-3}	1.70×10^{-3}	1.70×10^{-4}	80	2.47×10^{-7}
	2	1.20×10^{-3}				1.20×10^{-7}
	3	1.68×10^{-3}				1.67×10^{-7}
	4	1.30×10^{-3}				1.29×10^{-7}
PDFs		Bingham	Negative exponential	Negative exponential	Negative exponential	Truncated power law

In the truncated power law model, the simulated distributions of hydraulic conductivity in the low to intermediate range (cumulative probabilities: 0 to 50%) reproduce the measured data well. However, the simulation does not reproduce the higher permeable parts (hydraulic conductivity > 10^{-7}cm/s) well. That is, simulations with the truncated power law model underestimate frequency of high permeabilities in the rock mass at the Shobasama Site. The reverse is true for the negative exponential distributions. The comparison indicates that the truncated power law model and the negative exponential model successfully reproduce the lower permeability part and higher permeable parts, respectively.

For both models, simulated hydraulic conductivities decrease from the "Fracture zone along the fault" to the "Upper fracture zone", and decrease further in the "Moderately fractured zone". This tendency is the same as that of the measured values. Based on the fracture distribution parameters shown in Tables 4.22 and 4.23, the hydrogeological model was constructed using an equivalent continuum which takes the hydrogeological heterogeneity of the Shobasama Site into consideration.

(3) Construction of hydrogeological model

3-D finite element meshes were developed for the groundwater flow simulation, based on the geological units in the geological model and the 3-D distribution of permeable fractures described in the previous section. The following are taken into consideration.

① The topography is expressed by plane meshes.
② Geological formations and faults expressed in the geological model are expressed by 3-D meshes.
③ The shaft and galleries in the Tono Mine are expressed by nodal points or elements.
④ Locations of major boreholes are arranged to coincide with lattice points of the plane mesh.
⑤ Large-scale fracture zones are expressed by 3-D meshes, if necessary.

3-D meshes are formed, taking boundaries of the geological units shown in Table 4.24 into consideration. The 3-D meshes are shown in Figure 4.48. The number of elements and nodal points total 99,293 and 61,395, respectively.

Table 4.24 Geological units and hydraulic conductivities used for the homogeneous model

Geological units	Hydraulic conductivity (m/s)
Seto Group	1.0×10^{-7}
Oidawara Fm.	1.0×10^{-9}
Akeyo Fm.	1.0×10^{-8}
Toki Lignite-bearing Fm. (Upper)	5.0×10^{-9}
Toki Lignite-bearing Fm. (Basal conglomerate)	1.0×10^{-7}
Toki Granite (Weathered)	1.0×10^{-7}
"Moderately fractured zone"	1.0×10^{-9}
"Upper fracture zone"	2.0×10^{-8}
Tsukiyoshi Fault	1.0×10^{-10}
"Fracture zone along the fault"	1.0×10^{-7}

Using these meshes, the 3-D distribution of permeable fractures described in the previous section is statistically developed in the granite to construct an "equivalent continuum model". For each of the two fracture distribution models (truncated power law model and negative exponential model), a database of fracture distributions was developed. Figure 4.49 shows the 3-D comparison between the two models. Each block in the Figure is a cube with sides 60 m-long. It turns out that the truncated power law model develops more continuous fractures than the negative exponential model.

Figure 4.50 shows a homogeneous model, truncated power law model and negative exponential model. These three models are used for groundwater flow simulations. Here, "homogeneous model" refers to a model where a definite hydrogeological property is given to each of the geological formations without taking any heterogeneous permeability generated by fracture distributions into consideration.

In the homogeneous model (Figure 4.50(a)), hydraulic conductivity listed in Table 4.24 is applied to the finite element meshes shown in Figure 4.28. Most of the hydraulic conductivities applied to each geological unit are identical with those set for the 1st analysis loop (Table 4.13). However, hydraulic conductivities of the Akeyo Formation and the lower part of the Toki Lignite-bearing Formation were changed so that they would represent each element more precisely, with attention paid to contrasts in the geological units. Specifically, the Akeyo Formation is assigned a hydraulic conductivity of 1.0×10^{-8} m/s to represent its typical lithofacies of fine- to medium-grained sandstone. The Lower Toki Lignite-bearing Formation is assigned a hydraulic conductivity of 1.0×10^{-7} m/s because its highly permeable basal conglomerate has the same hydraulic conductivity as the weathered zone of the granite, i.e., 1.0×10^{-7}m/s. The hydraulic conductivities of the "Upper fracture zone", "Moderately fractured zone" and "Fracture zone along the fault" were based on the results of hydraulic tests carried out in MIU-1, 2 and 3.

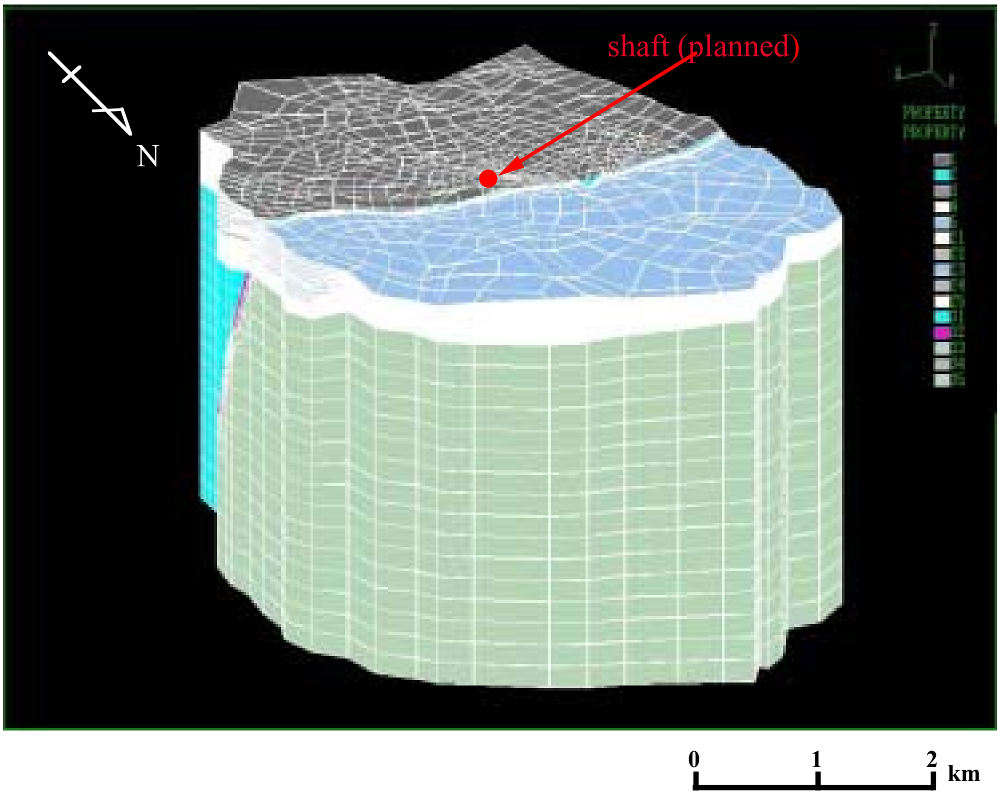

Figure 4.48 3D finite element mesh

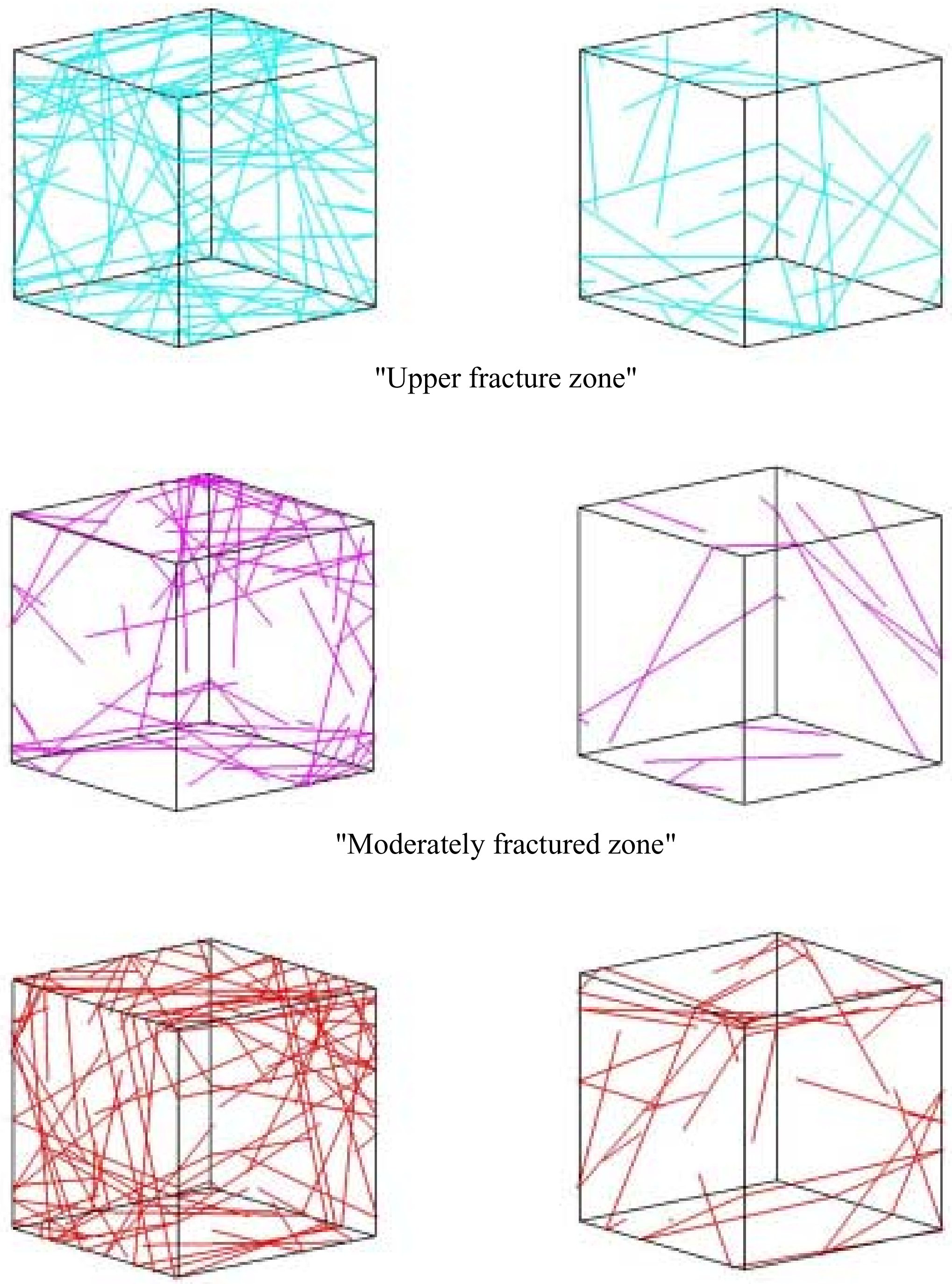

(a) Truncated power law model (b) Negative exponential model

Figure 4.49 Comparison of fracture distribution between two models

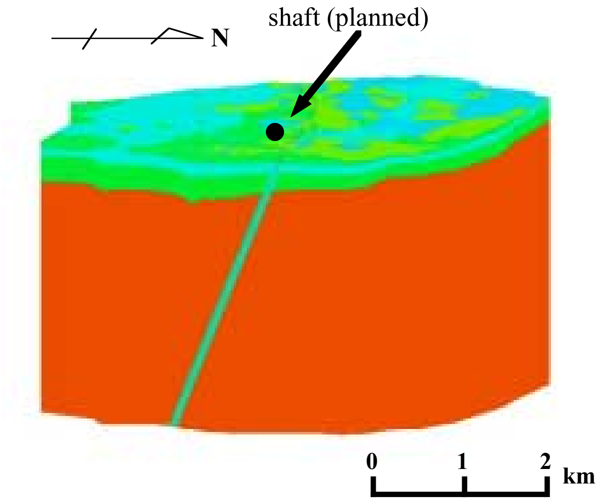

(a) Homogeneous model

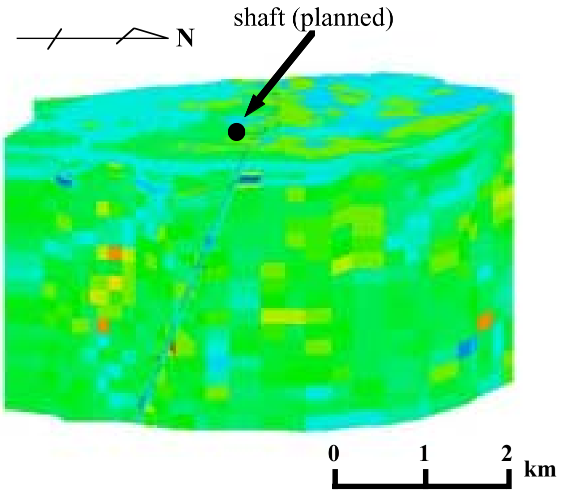

(b) Truncated power law model

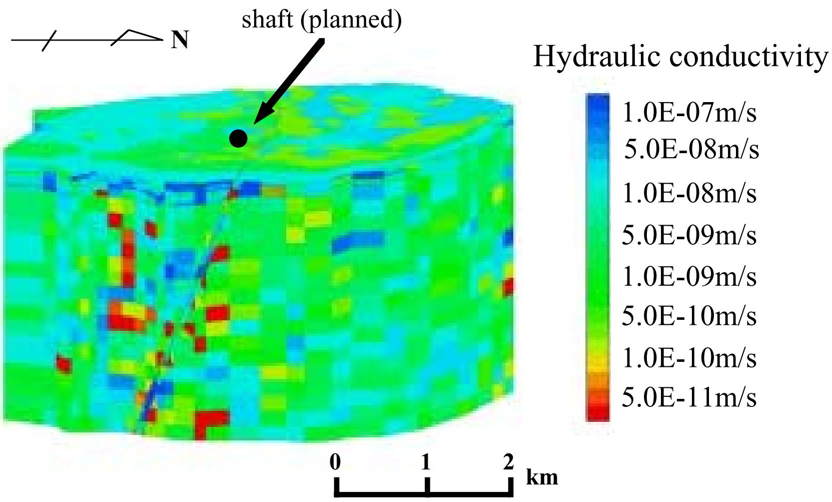

(c) Negative exponential model

Figure 4.50 Hydraulic conductivity distribution (a bird's-eye view)

Hydraulic boundary conditions for simulation are set as follows:

① Top boundary condition (Ground surface)

Based on the investigations and analyses described in Section 4.2.2.2 **Establishing boundary conditions**, the recharge rate at ground surface was established for the top boundary. The recharge rate of 0.28mm/day, the mean calculated from observations carried out from 1990 to 1997 in the vicinity of the Tono Mine, and employed for the RHS Project was applied to a groundwater simulation (steady-state). The results are compared with the data from groundwater monitoring in boreholes. The results show head distribution derived by the simulation has higher values than the actual observations. While this is presumably due to the calculated recharge rate and/or the head values assigned to the side boundaries, the reason has yet to be specified. Thus, on the assumption that the recharge rate used exerts a greater influence on the results of simulation, the recharge rate was amended to 0.14mm/day so that the simulated results would match the observed data. Taking spring water into consideration, the ground surface is postulated as a free seepage surface with unrestricted inflow and outflow of water possible. The determination of the recharge rate will be examined in more detail in future studies.

② Bottom boundary condition

The bottom boundary is set as a no-flow boundary.

③ Side boundary conditions

The side boundaries are considered to be groundwater flow divides. Three coincide with mountain ridges, the northern, eastern and western boundaries and are assigned constant head values to depth, as a permeable boundary. The constant head values assigned to the side boundaries are calculated by the following formula between the water level data in boreholes and elevations of the ground surface:

$$\Phi \text{ (constant head value)} = 0.86 \times H \text{ (elevation of each location)} + 18.5.$$

The boundary along the Toki River (southern boundary) is also assigned a definite hydrostatic head as a permeable boundary. The elevation of the river surface is used as the constant head values assigned to the southern boundary.

④ Galleries of the Tono Mine and the MIU shafts

Since the Tono Mine's galleries are modeled using nodal points exposed to atmospheric pressure, the constant head value is set as the pressure head of 0 m. As for the MIU shafts modeled using elements, corresponding elements are deleted from the hydrogeological model with the advance of planned shaft excavation. Nodal points corresponding with the shaft wall after excavation are regarded as free seepage points.

4.2.3.3.5 Groundwater flow simulation

The groundwater flow simulation adopts the saturated/unsaturated seepage flow analysis code (EQUIV-FLO) for an equivalent heterogeneous continuum (heterogeneous porous media). This code has governing equations including Darcy's law taking unsaturated domains and saturated flow conditions into consideration using the continuity equation for groundwater flow in porous media (conservation of mass

Hydraulic boundary conditions for simulation are set as follows:

① Top boundary condition (Ground surface)

Based on the investigations and analyses described in Section 4.2.2.2 **Establishing boundary conditions**, the recharge rate at ground surface was established for the top boundary. The recharge rate of 0.28mm/day, the mean calculated from observations carried out from 1990 to 1997 in the vicinity of the Tono Mine, and employed for the RHS Project was applied to a groundwater simulation (steady-state). The results are compared with the data from groundwater monitoring in boreholes. The results show head distribution derived by the simulation has higher values than the actual observations. While this is presumably due to the calculated recharge rate and/or the head values assigned to the side boundaries, the reason has yet to be specified. Thus, on the assumption that the recharge rate used exerts a greater influence on the results of simulation, the recharge rate was amended to 0.14mm/day so that the simulated results would match the observed data. Taking spring water into consideration, the ground surface is postulated as a free seepage surface with unrestricted inflow and outflow of water possible. The determination of the recharge rate will be examined in more detail in future studies.

② Bottom boundary condition

The bottom boundary is set as a no-flow boundary.

③ Side boundary conditions

The side boundaries are considered to be groundwater flow divides. Three coincide with mountain ridges, the northern, eastern and western boundaries and are assigned constant head values to depth, as a permeable boundary. The constant head values assigned to the side boundaries are calculated by the following formula between the water level data in boreholes and elevations of the ground surface:

$$\Phi \text{ (constant head value)} = 0.86 \times H \text{ (elevation of each location)} + 18.5.$$

The boundary along the Toki River (southern boundary) is also assigned a definite hydrostatic head as a permeable boundary. The elevation of the river surface is used as the constant head values assigned to the southern boundary.

④ Galleries of the Tono Mine and the MIU shafts

Since the Tono Mine's galleries are modeled using nodal points exposed to atmospheric pressure, the constant head value is set as the pressure head of 0 m. As for the MIU shafts modeled using elements, corresponding elements are deleted from the hydrogeological model with the advance of planned shaft excavation. Nodal points corresponding with the shaft wall after excavation are regarded as free seepage points.

4.2.3.3.5 Groundwater flow simulation

The groundwater flow simulation adopts the saturated/unsaturated seepage flow analysis code (EQUIV-FLO) for an equivalent heterogeneous continuum (heterogeneous porous media). This code has governing equations including Darcy's law taking unsaturated domains and saturated flow conditions into consideration using the continuity equation for groundwater flow in porous media (conservation of mass law) [70]. The 3-D steady-state/transient groundwater flow simulation was carried out from the viewpoint of the known hydrology with existing galleries of the Tono Mine and the predicted hydrology affected by the excavation of the MIU shafts.

(1) Simulation cases

Simulation cases were set as follows.

- Case 1 : steady-state homogeneous model
- Case 2 : steady-state truncated power law model
- Case 3 : steady-state negative exponential model
- Case 4 : transient homogeneous model
- Case 5 : transient truncated power law model
- Case 6 : transient negative exponential model

The excavation schedule of the shaft, which was used for the above transient simulations, was set as shown in Table 4.25. This schedule not only respects the work schedule [71] planned in 1998 FY but also takes the mesh structure of the hydrogeological model into consideration.

Table 4.25 Assumed schedule of shaft excavation

Stage	Depth (m)	Elevation (m)	Cumulative time (days)
2	21.8	209.635	39.1
3	41.0	190.435	73.5
4	60.2	171.235	108.0
5	79.4	152.035	142.4
6	101.8	129.635	182.6
7	145.3	86.135	260.8
8	205.9	25.535	369.4
9	266.4	-34.965	478.1
10	306.8	-75.365	550.1
11	327.0	-95.565	586.7
12	508.5	-277.065	912.5
13	508.5	-277.065	1,460.0
14	690.0	-458.565	1,638.0
15	871.5	-640.065	2,099.0
16	1,001.4	-769.965	2,250.0

(2) Results of the steady-state simulations

Steady-state simulations were carried out with the purpose of understanding the current groundwater hydrogeology in the study area and investigating initial conditions to predict effects of the shaft excavation. The results of simulations using the three models are shown in Figures 4.51, 4.52, 4.53 and 4.54. These show water pressure distribution from several perspectives, including a bird's-eye view, pressure distribution in horizontal sections, the pressure distribution in different vertical sections and the comparison between simulated and measured data of head and water pressure, respectively. The major results are as follows.

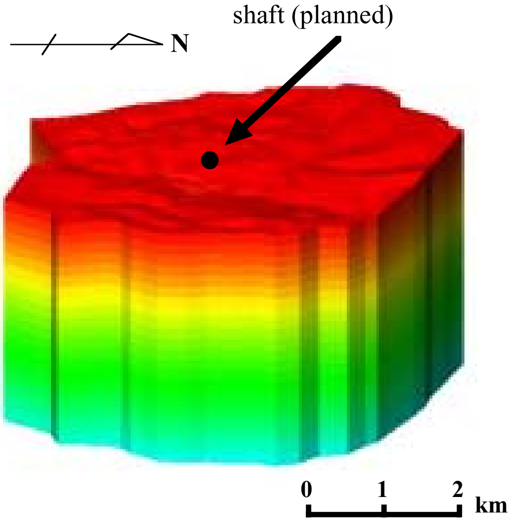

(a) Homogeneous model

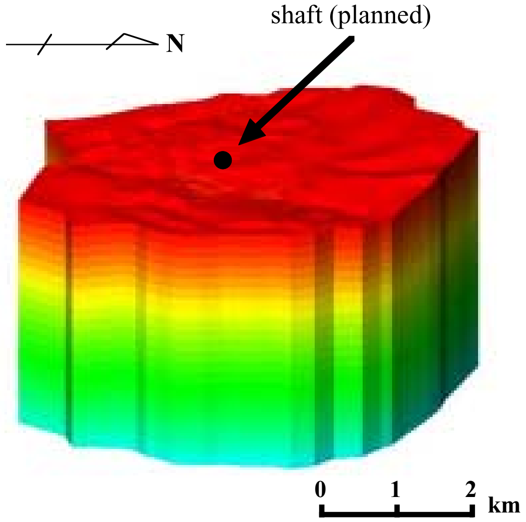

(b) Truncated power law model

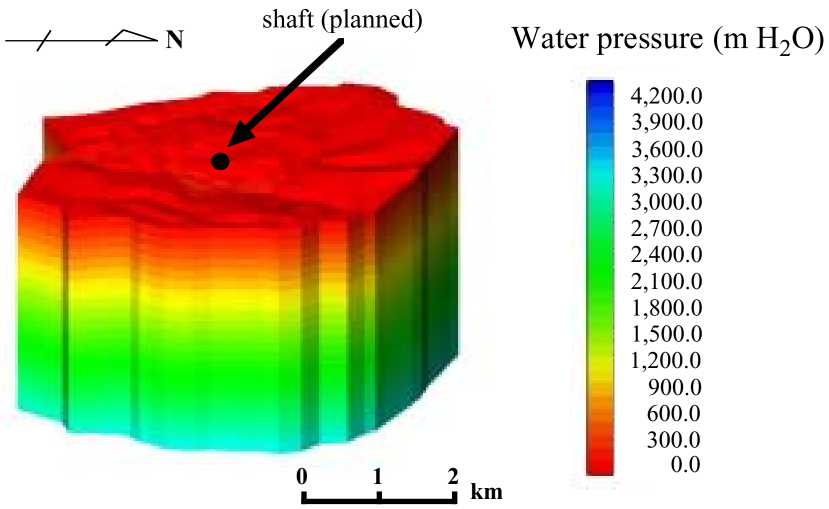

(c) Negative exponential model

Figure 4.51 Water pressure distribution (a bird's-eye view)

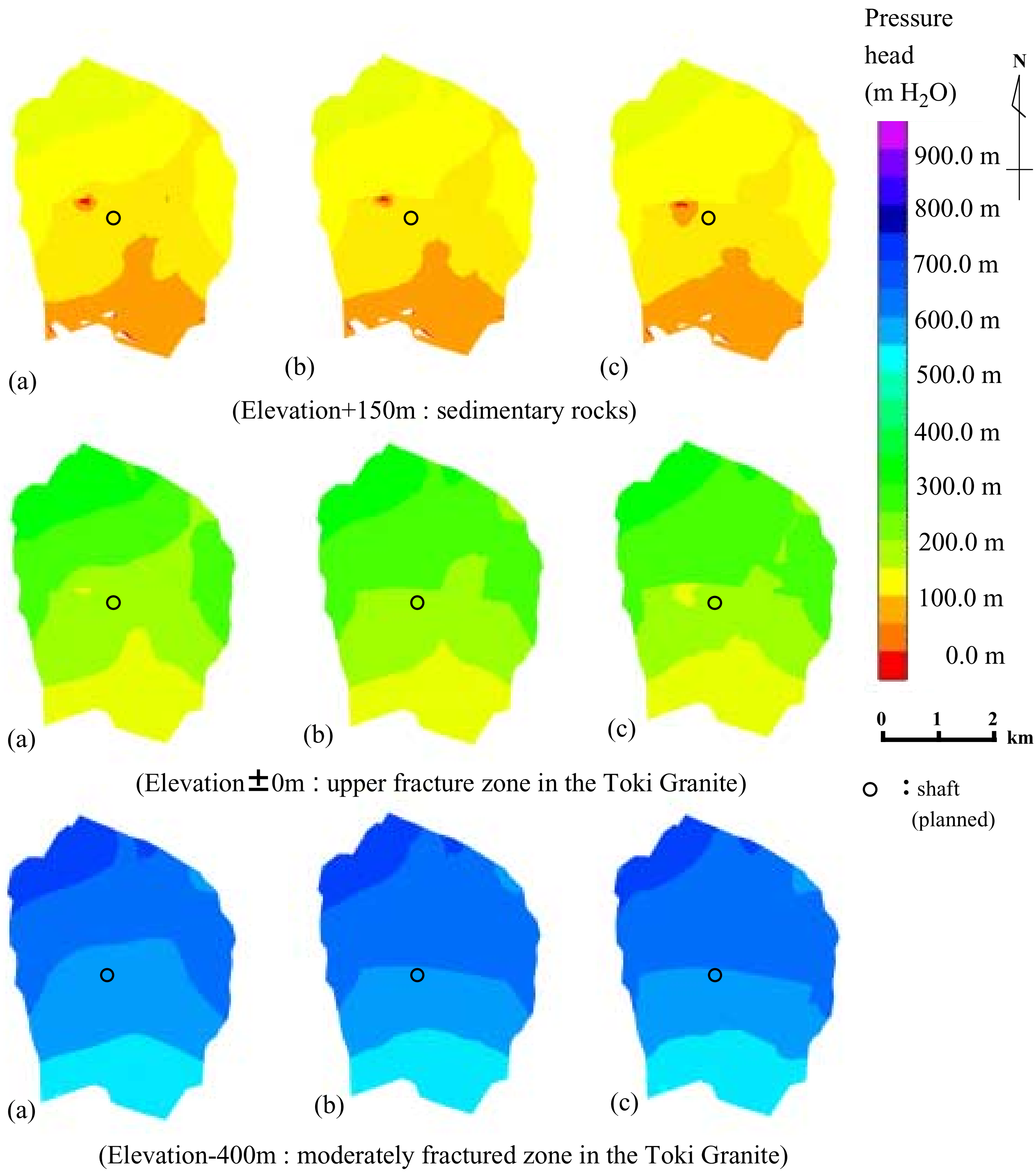

((a) Homogeneous model, (b) Truncated power law model, (c) Negative exponential model)

Figure 4.52 Pressure head distribution in horizontal plane

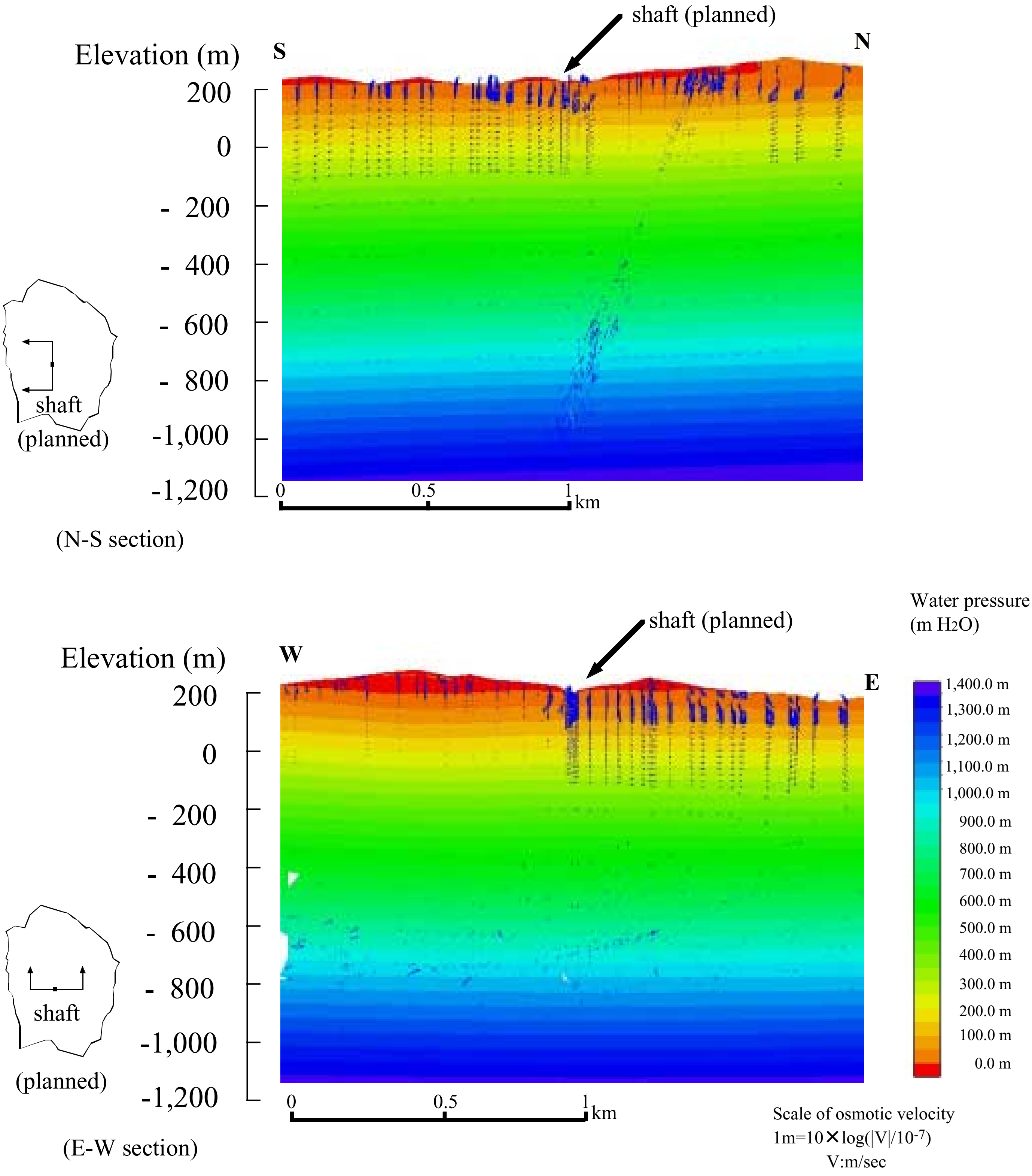

(a) Homogeneous model

Figure 4.53 Water pressure distribution in vertical section (1)

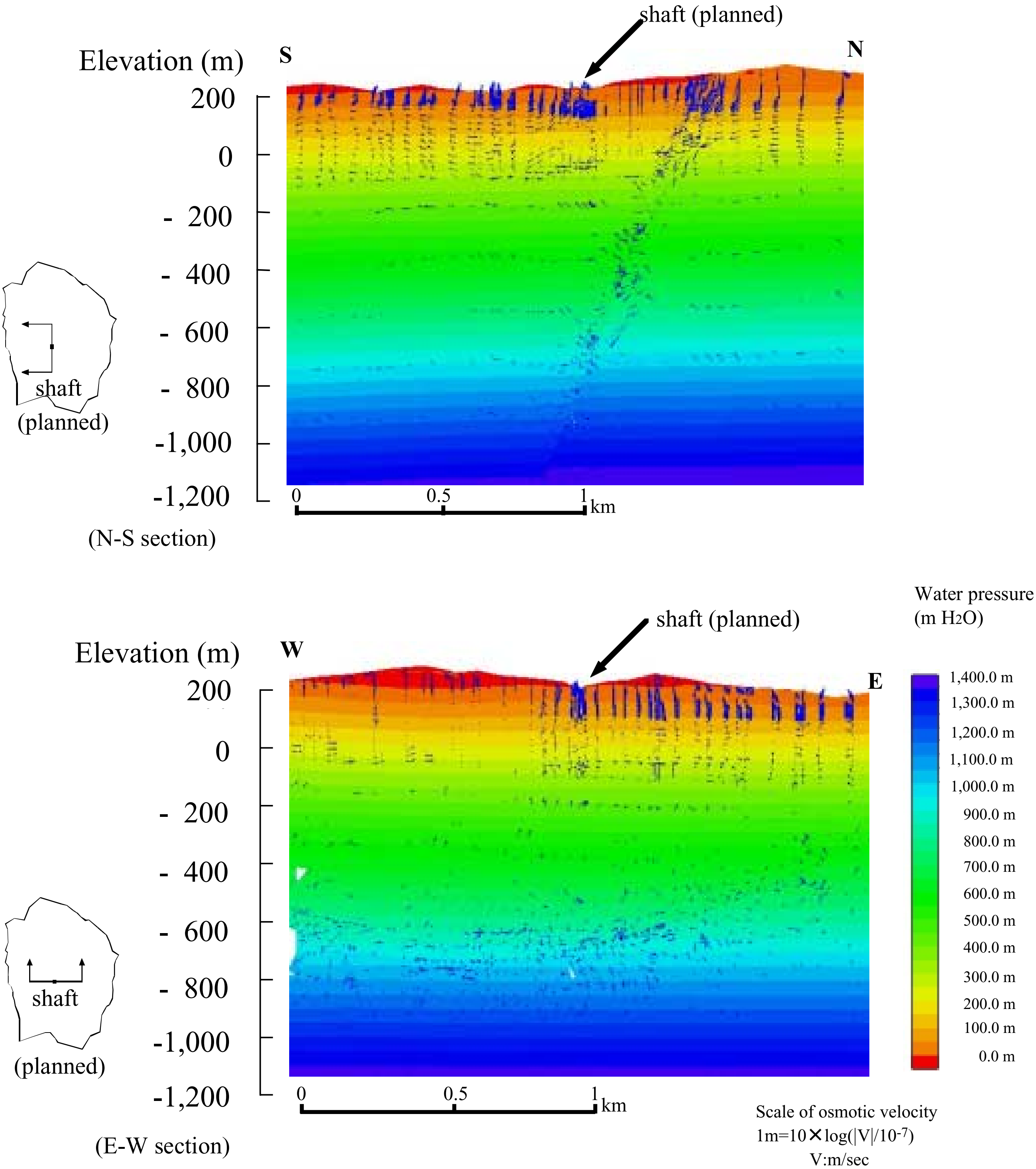

(b) Truncated power law model

Figure 4.53 Water pressure distribution in vertical section (2)

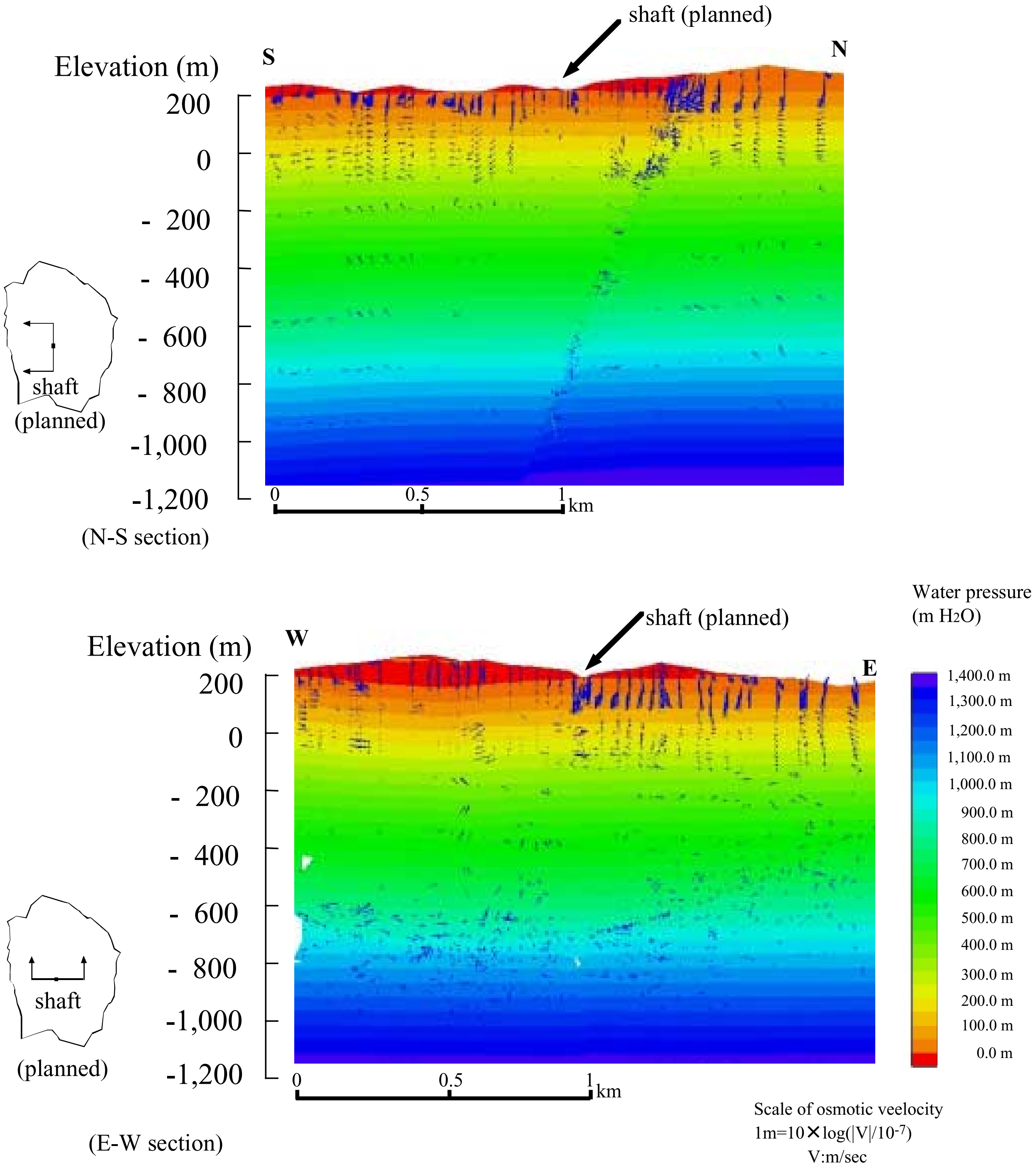

(c) Negative exponential model

Figure 4.53 Pressure head distribution in vertical section (3)

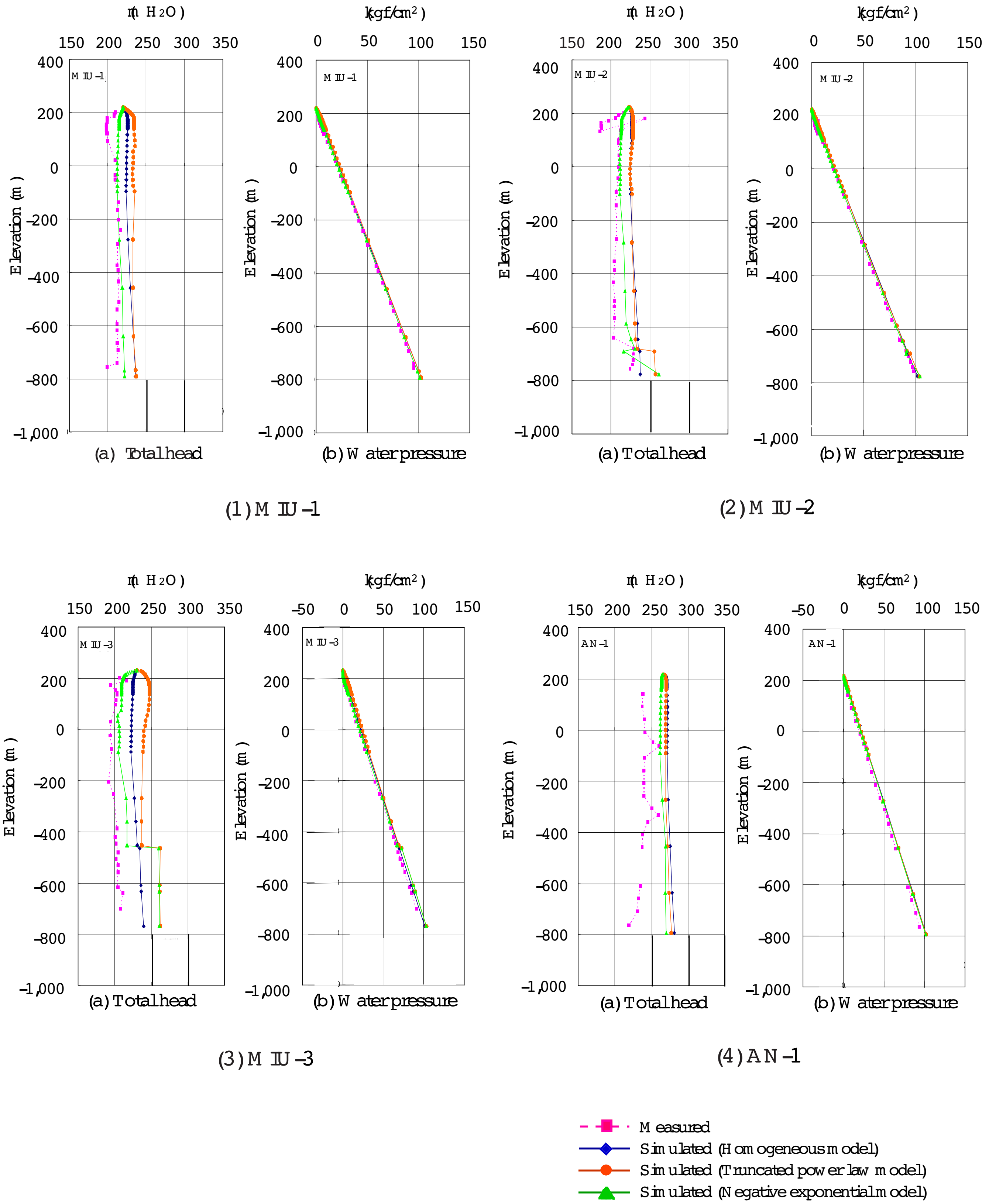

Figure 4.54 Comparison between simulated data and measured data of total head and water pressure

① Head distributions in all the models indicate that the groundwater flow potential is from the northern side (mountain area) to the southern side (the Toki River) of the study area.

② In shallow parts, local topographical effects are seen; exemplified by a groundwater flow along the Hiyoshi River running from north to south on the east side of the study area (Figures 4.52, 4.53). Topographical effects on the pressure distribution reduce with depth, resulting in a dominant flow from north to south.

③ The groundwater flow simulation using the hydrogeological model in the 1st analysis loop fails to reproduce a barrier to flow effect across the Tsukiyoshi Fault. However, the hydrogeological model (homogeneous model) in the 2nd analysis loop does reproduce the barrier to flow effect.

④ All of the models used in the 2nd analysis loop more or less show a barrier-to-flow effect of the Tsukiyoshi Fault on the southward groundwater flow. Especially, the barrier-to-flow effect of the fault in the sedimentary rocks and the "Upper fracture zone" of the granite are shown in Figure 4.52. In the "Moderately fractured zone" remarkable barrier-to-flow effects of the fault were recognized in the truncated power law model and the negative exponential model, whereas it is less distinct in the homogeneous model. It is presumed to be due to a small difference in hydraulic conductivity in the model between the fault (10^{-10} m/s) and the "Moderately fractured zone" (10^{-9} m/s). On the other hand, the logarithmic mean of hydraulic conductivities of the "Moderately fractured zone" is set at 10^{-9} m/s. in both of the truncated power law model and negative exponential model. However, the hydraulic conductivity varies so widely that it can be as high as 10^{-6}m/s. in parts where fractures are concentrated or fractures with large opening widths occur. Thus, the barrier-to-flow effect of the fault probably appears more distinctly in the truncated power law model and negative exponential model than in the homogeneous model.

⑤ Flow rate in the granite varies in a narrow range in the homogeneous model, whereas highly permeable fractures generate locally fast groundwater flow in the truncated power law model and the negative exponential model (Figure 4.53).

⑥ Heads (measured) in the MIU-1, 2 and 3 are basically equal to hydrostatic pressures. On the other hand, heads in MIU-2 and 3, where the Tsukiyoshi Fault is intersected, change abruptly on opposite sides of the fault (Figure 4.54). Especially in MIU-2, the head on the footwall side of the fault is some 30 m higher than that on the hanging wall side, when converted to water level. While simulated values are generally higher than the measured ones, generally they are more conformable in the negative exponential model than in the other models. Also, pressure rise on the footwall side of the fault in MIU-3 was not measured. This is presumed to be due to a drop in water pressure caused by the penetration of the fault by MIU-2. Head values obtained by the homogeneous model are intermediate between those obtained by the truncated power law model and the negative exponential model (Figure 4.54).

⑦ The water pressure distributions in AN-1 and 3 in the southern part of the Shobasama Site are nearly hydrostatic. In AN-1, sections with locally high and locally low measured heads occur at depth. However, the simulations fail to reproduce these local variations in measured values. Furthermore, simulated heads are generally higher than measured ones.

(3) Results of the transient simulations

Results of the simulations in the following two stages out of the 16 shown in Table 4.25 are discussed below.

① Stage-13 : Left to stabilize for about one and half years after excavation to 508.5 m in depth

② Stage-16 : Shaft excavation is completed to 1,001.4 m depth after penetrating the Tsukiyoshi Fault

Effects of the shaft excavation on water pressure distribution in Stage-13 (shaft 508.5 m)

Stage-13 represents the point when the shaft is excavated to about half its total depth. Vertical profiles of the water pressure distribution shown in Figure 4.55 indicate that the shaft excavation causes a drop in the adjacent water pressure in all models. Furthermore, a lowering of water level around the shaft is wider than the stage prior to the excavation (Figure 4.53).

A cone-shaped drop in water pressure develops around the shaft in the homogeneous model (Figure 4.55 (a)). On the other hand, an asymmetric shape in the drop forms in both the truncated power law model and the negative exponential model (Figures 4.55 (b), (c)). These are created by the excavation effects propagated along permeable fractures intersected by the shaft. Especially, in the truncated power law model containing fractures with a large diameter (Figure 4.55(b)), extensive pressure drops are formed by fractures in the “Upper fracture zone” intersected by the shaft. The pressure drop also develops along fractures in the negative exponential law model (Figure 4.25(c)). However, the frequency of large fractures in this model is lower than the frequency in the truncated power law model, resulting in smaller pressure drops.

Effects of the shaft excavation, which is done entirely in the hanging wall to this point, do not extend beyond the Tsukiyoshi Fault in any models, hardly extend to the north side of the fault (Figures 4.55, 4.56). On the other hand, the pressure drop zone extends east and west, forming a striking contrast to the pressure distributions along the north-south profiles that feature an abrupt change at the fault (Figures 4.55, 4.56). The distribution of flow velocity vectors of groundwater in the north-south profiles indicates that water is supplied into the shaft from the ground surface and at depth through fractured zones around the fault. The truncated power law model and negative exponential model occasionally develop concentrated flows through fractures from the fractured zones around the fault toward the shaft.

Pressure distributions in the horizontal sections at elevations of +150 m and ±0 m above the shaft bottom (GL-508.5m; at an elevation of -277.0 masl) show a pressure drop around the shaft (Figure 4.56). The pressure drop area at an elevation of +150 m forms a concentric circle around the shaft in the homogeneous model (Figures 4.55, 4.56). However, the extent is too limited to exert an influence on the initial pressure distribution of the Tono Mine. The pressure drop in the truncated power law model affects the largest area among the three models, extending to the Tono Mine and the Shobasama Site. It is probably because the pressure drop along fractures in the granite has a large effect on the groundwater flow in the shallow part. The pressure drop area in the negative exponential model is not as large as in the truncated power law model. However, it extends to the pressure drop area of the Tono Mine. Excavation effects of the shaft are found at an elevation of ±0 masl, too. The pressure drop area around the shaft in the homogeneous model is also linked with the pressure drop area around the Tono Mine. The effect, however, scarcely extends onto the north side of the fault. The affected area in the truncated power law model is the largest among the three models, partially extending to the north side of the fault, too. It is probably because parts of the fractures extend northward across the fault. Though fractures across the fault have yet to be ascertained, this gives a suggestion on the extent of potential excavation effects of the shaft when such fractures are actually verified. No effect of the pressure drop at an elevation of ±0 masl extends to the north across the fault in the negative exponential model. It is probably because there are fewer fractures with a large diameter in the negative exponential model than in the truncated power law model. Effects of the shaft excavation gradually lessen beneath the borehole bottom, scarcely found at an elevation of -600 masl except in the truncated power law model. In the truncated power law model, however, a small pressure drop area occurs even at an elevation of –700 masl, extending northward across the fault. This indicates that large fractures in the “Upper fracture zone” in the granite exert an extensive influence on pressure drop horizontally as well as vertically.

Effects of the shaft excavation on water pressure distribution in Stage-16 (shaft bottom 1001.4 m)

Stage-16 represents the point when the shaft excavation is completed after penetrating the Tsukiyoshi Fault. In this stage changes in water pressure extend into the footwall, the north side of the fault in all of the models (Figures 4.57, 4.58). In the homogeneous model, above all, a conical pressure drop domain extends on the both north and south sides of the fault to show a radial symmetry (N-S, E-W). This is thought to be caused by penetration of the fault by the shaft (Figure 4.58).

The water level distribution at excavation levels shallower than –300 masl on both the north and the south sides of the fault does not show a big change after the excavation extends below 508 m depth (Stage-13), (Figures 4.55, 4.57). This indicates that the shaft excavation influence on the water level in the shallow parts is reduced above an elevation of -300 m, as soon as the shaft passes through the sedimentary rocks and the “Upper fracture zone” of the granite. The water flows along the “Fracture zone along the fault” are more remarkable in Stage 16 than in Stage-13, directly pouring into the shaft.

The horizontal sections of pressure distribution show pressure drops on the north side of the fault in the truncated power law model and negative exponential model, which can be attributed to penetration of the fault by the shaft. However, they are not as extensive as in the homogeneous model (Figure 4.58). This indicates that the barrier-to-flow effect of the fault in the rock mass with homogeneous permeability differs from that in the rock mass with heterogeneous permeability. That is, it is presumable that effects of a pressure drop due to shaft excavation selectively propagate through highly permeable fractures in the heterogeneous model, whereas they almost concentrically (radially) spread in the homogeneous model. The magnitude of pressure drop area around the shaft, at an elevation of -600 masl (831.5 m depth), decreases in sequence from the homogeneous model to the truncated power law model and last to the negative exponential model. The order is the same as that of the fracture continuity.

There is little change in patterns of pressure distribution at an elevation of ±0 masl (231.44 m depth) between Stage-13 and Stage-16. Pressure drop areas develop around the shaft below an elevation of -400 m. The difference in pressure distribution among the three models is not as large as in the shallow part. It is probably because this section is in the "Moderately fractured zone", has fewer fractures and especially fewer fractures with large diameters.

(4) Summary

Results of the construction of the hydrogeological model and groundwater flow simulation are summarized as follows.

① In the 2nd analysis loop, homogeneous, truncated power law and negative exponential models were constructed. They were constructed on the basis of the data on fracture distribution and hydraulic conductivity obtained in the 1,000 m-deep MIU-1, 2 and 3 boreholes drilled inside the Shobasama Site. The truncated power law model is more dispersed in fracture diameter than the negative exponential model, that is, it contains fractures with larger diameter. The negative exponential model is aimed at a better reproduction of the heterogeneity in measured hydraulic conductivity and is characterized by a lower 1-D fracture density.

② No remarkable difference is found in groundwater flow prior to the shaft excavation between the homogeneous model (<u>no</u> fractures taken into consideration) and truncated power law model and negative exponential model (taking fractures into consideration).

③ The shaft excavation generates a conical pressure drop field around the shaft in the homogeneous model. On the other hand, it generates irregular pressure drop fields along the fractures in the other models. There is no large difference in effects of the shaft excavation in the "Moderately fractured zone" between the homogeneous model and the other models.

④ No effect of shaft excavation extends to the north side of the fault until the shaft penetrates the fault. After penetration, a pressure drop forms on the footwall side (north side) of the fault. The extent of the effect depends on the distribution of fractures. The present simulation indicates that an "equivalent continuum model" (model which takes the heterogeneities into consideration) has a more restricted extent of pressure drop. It probably results from the heterogeneities of hydraulic conductivity.

⑤ The "equivalent continuum model" allows representation of the fracture distribution (direction, density, size and permeability) in the hydrogeological model. Therefore, the "equivalent continuum model" can reproduce the low permeability of the Tsukiyoshi Fault, and is applicable as a methodology for evaluating the groundwater hydrogeology of a several km^2 area.

4.2.4 Future tasks

The results of the 1st analysis loop allow overall understanding of groundwater flow. However, their comparison with the measured values obtained through the subsequent borehole investigations indicated a large discrepancy in the head distribution in the granite. Furthermore, an important task recognized was to determine the cause of the discrepancy and the prioritization of data acquisition in order to reduce the uncertainty of the simulated results.